IEEE Access
Multidisciplinary ⋮ Rapid Review ⋮ Open Access Journal

Received 1 May 2024, accepted 21 May 2024, date of publication 30 May 2024, date of current version 7 June 2024.

Digital Object Identifier 10.1109/ACCESS.2024.3407605

RESEARCH ARTICLE

Deep Learning Stack LSTM Based MPPT Control of Dual Stage 100 kWp Grid-Tied Solar PV System

UMAIR YOUNAS[1], AHMET AFSIN KULAKSIZ[1], AND ZUNAIB ALI[2], (Member, IEEE)
[1]Department of Electrical and Electronics Engineering, Konya Technical University, 42250 Konya, Turkey
[2]London Centre for Energy Engineering (LCEE), School of Engineering, London South Bank University, SE1 0AA London, U.K.

Corresponding author: Zunaib Ali (aliz29@lsbu.ac.uk)

ABSTRACT Rising global energy demand, predominantly satisfied by fossil fuels, triggers fuel price surges, fuel scarcity, and substantial greenhouse gas emissions. Solar photovoltaics (PV), as an abundant renewable alternative, can potentially address this demand, yet low cell efficiency (15-25%) and fluctuating output power due to intermittent irradiance (G) and temperature (T) impedes grid integration. This paper presents a novel Deep Learning (DL) based stacked LSTM (Long Short-Term Memory) MPPT controller to maximize power harvesting from a 100 kW grid-tied solar PV system, demonstrating superiority over conventional Perturb & Observe (P&O) and Feed Forward-Deep Neural Network (FF-DNN) MPPT approaches. Subsequently, a Neutral-Point-Clamped (NPC) 3-level inverter with proportional-integral (PI) controllers regulates the DC link voltage and transfers the extracted PV power to the grid. The proposed MPPT methodology includes collection of one million-sample (G, V, Vmp) datasets; preprocessing via z-score normalization; visualizing distributions through histograms and correlation matrix plots; an 80/20 split rule-based training and test sets; a two-hidden layer stacked LSTM (64 and 32 neurons) architecture; hyperparameters including the Adam optimizer, 0.05 learning rate, 32 batch size, and 50 epochs. Model efficacy quantification uses MSE, RMSE, MAE, loss, and R2 metrics. For 100 kW generated PV power, the stacked LSTM extracts 98.2 kW, versus 96.1 kW and 94.3 kW for the DNN and P&O MPPTs respectively. By integrating the optimized proposed stack LSTM MPPT with a streamlined inverter topology, the proposed approach advances the state-of-the-art in DL based solar PV energy harvesting optimization and grid integration.

INDEX TERMS Deep learning, grid integration, long short-term memory network, maximum power point tracking, solar photovoltaic, deep neural network.

I. INTRODUCTION

Rising global energy demand originated from population growth, industrialization, and urbanization [1]. This massive energy demand is nevertheless largely fulfilled by conventional fossil fuels like coal, natural gas, and oil as demonstrated in Fig. 1 [2]. However, the adverse environmental impact coupled with fuel price volatility and finite fossil fuel reservoirs necessitates the integration of renewable alternatives like solar photovoltaics (PV) to fulfil the global rising energy demand [3]. Although solar PV systems are clean, noiseless, economical, and abundant energy sources [4], PV integration into the grid faces barriers like low solar cell efficiency, variable PV output power due to intermittent sun irradiance (G) and solar cell temperature (T), power conversion losses, harmonics due to DC link voltage instability and complexity in grid synchronization. The increasing adoption of advanced MPPT and inverter control topologies has significantly improved the efficiency of grid-connected PV systems, as evidenced by the rapid growth in installation of the PV panels over the past few decades as shown in Fig. 2 [5]. The two predominant solar

The associate editor coordinating the review of this manuscript and approving it for publication was Ton Duc Do.

PV system configurations are grid-connected and off-grid. Off-grid systems are independent of the utility grid and attain energy autonomy via battery storage, making them better suited for remote locales regardless of the higher initial cost. Grid-connected systems establish integration with the utility grid, feeding surplus power back to the grid while drawing energy from it when solar generation is deficient. By utilizing existing infrastructure, grid-connected systems are prevalent in residential and commercial applications with lower upfront expenditures [6]. The dual stage grid-connected architecture employed in this article encompasses PV arrays, MPPT controller, DC/DC converters, inverters, LCL filters, PLL synchronization, and utility microgrid. The first stage tracks and harvests the maximum available PV power from the PV panel in the presence of dynamic G and T values, while the second stage transfers the harvested power to the grid by ensuring the DC link voltage regulation and grid synchronization.

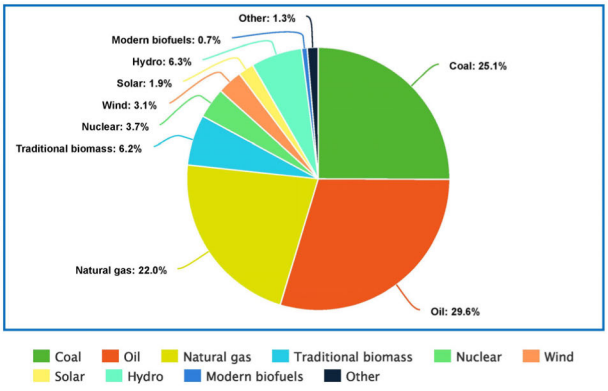

FIGURE 1. Shares of global energy demand.

In the literature, researchers have explored a spectrum of MPPT approaches, including traditional methods, smart techniques, and Machine Learning (ML) based MPPT controllers to support the intermittent PV power generation caused by fluctuations in G and T values in dual stage grid tied PV systems.

A literature survey on the traditional MPPT methods emphasizes that the Perturb and Observe (P&O) method is simple and has low computational complexity using only a single voltage or current sensor [7], [8]. However, due to its iterative nature of constantly perturbing the operating point, it tends to fluctuate around the maximum power point (MPP) under dynamic conditions. In contrast, Incremental Conductance (IC) method reduces the fluctuations by dynamically adjusting the operating point according to power and voltage or current changes [9], but it slightly increases the complexity by using two sensors compared to the P&O method and also encounters fluctuations around the MPP during rapid weather variations. The Open Circuit Voltage (OCV) method further simplifies the system by utilizing the characteristics of PV modules without the need for additional sensors or complex algorithms. However, authors in [10] stated that accuracy decreases under changing environmental conditions due to its reliance on static voltage/temperature curves. The Short Circuit Current (SCC) MPPT method also reduces the system complexity by using a single current sensor [11] but it also exhibits drawbacks like oscillations, slow convergence, and sensitivity to rapidly changing conditions.

The challenges of traditional MPPT methods have motivated researchers to delve into smart MPPT algorithms including Fuzzy Logic Controllers (FLC), Particle Swarm Optimization (PSO), Genetic Algorithm (GA), Artificial Neural Networks (ANN), and Machine Learning based MPPT algorithms etc. Unlike traditional MPPT methods, Fuzzy Logic Controllers (FLC) use rule-basis to dynamically adjust the control parameters based on the degree of membership for input variables, thereby allowing more precise tracking and mitigation of oscillations around MPP [12]. However, FLC encounters difficulties during rapid changes in G and T due to its limited ability to capture complex relationships between input variables and optimal control actions due to static member functions. Particle Swarm Optimization (PSO) optimizes the duty cycle for enhanced MPP tracking efficiency through iterative updates of particle positions, influenced by individual best-known positions and collective knowledge of the swarm [13]. However, during rapid environmental changes, particles in PSO fail to adjust their positions quickly, leading to suboptimal performance in tracking the MPP. Genetic Algorithms (GA) based MPPT tackles slow adaptation by exploring a wider search space through evolutionary operations like selection, crossover, and mutation, enhancing optimization during rapid environmental changes [14]. However, it has limited adaptability to complex data relationships due to fixed operations and slower convergence rates. The ANNs which are building blocks of ML and DL algorithms outperform existing traditional and smart MPPT methods in terms of accuracy and efficiency. ANN learns complex patterns from inputs and target data set, continuously improves models based on new data, and dynamically optimizes MPPT accuracy and efficiency [15]. However, challenges remain regarding interpretability, overfitting, and dynamic adaptability. This necessitates hybrid, advanced ML, and Deep Learning (DL) based MPPT methods to further enhance the performance of MPPT controllers.

To address the challenges of the traditional and smart MPPT algorithms like sensitivity, complexity, and slow response time, researchers investigated hybrid MPPT methods which combine the features of the smart and conventional MPPT algorithms to utilize their complementary strengths. The authors in [16] integrated the ANN and Hill Climbing (HC) methods to address partial shading issues. This integration enables the ANN to learn complex data relationships, while HC refines the search process to converge towards the optimal solution, improving overall tracking accuracy. The authors in [17] optimized a standalone PV system with a GA-ANN approach. Here, GA offers a global search capability to explore the solution space

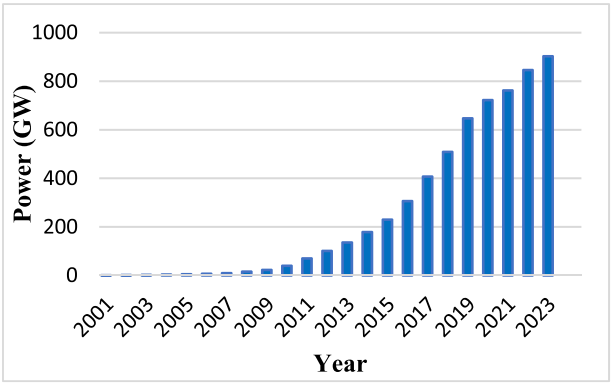

FIGURE 2. Installed capacity of solar PV generation.

effectively. While ANN offers adaptive learning to fine-tune the MPPT algorithm based on real-time data, enhancing system performance under varying conditions. PSO-ANFIS based hybrid MPPT model for hybrid microgrids is presented in [18]. In this integration, PSO optimizes the parameters of an Adaptive Artificial Neuro Fuzzy Inference System (ANFIS). It combines PSO's global search ability with ANFIS's to handle uncertain and nonlinear data, resulting in robust MPPT performance. Despite the advantages, hybrid MPPT approaches rely on predefined rules or parameters, and encounter slow convergence and lack in dynamic adaptability to varying environments. Thus, the integration of advanced DL-based MPPT approaches with superior data processing and adaptive learning capability is essential to surpass the performance of the state-of-the-art MPPT methods.

The challenges in traditional, intelligent and hybrid methods and the need for advanced MPPT algorithms have been demonstrated previously. In this section, we comprehensively compare the advantages, disadvantages and progressions in advanced ML and DL-based data-driven MPPT approaches, which are closely related to the proposed stacked LSTM MPPT method. Despite the growing interest in Artificial Intelligence (AI) for renewable energy systems, few studies have explored the potential use of DL for solar PV power optimization - a significant research gap that the proposed study aims to address with a stack LSTM-based MPPT tracking approach. The authors in [19] employed two Deep Neural Network (DNN) controllers in the category of Feed Forward Neural Network (FF-NN) controllers for a 40 kW solar/wind hybrid power system, including a custom DNN MPPT with 66,000 data points, two inputs, one output, and 1000 hidden neurons. The authors encourage the deployment of DNNs in PV/wind applications, but this simulation-based approach increased the computational overhead by using two distinct DNNs, with a larger number of hidden neurons for a small dataset of 66000 samples. In addition, the data preprocessing and visualization steps are missing which are essential for data-driven DNN approaches. The authors in [20] proposed a Recurrent Neural Network (RNN) MPPT algorithm for grid-connected PV, emphasizing cell temperature adaptation. However, key details like dataset size and model structure are not considered. In addition, despite RNN being a data-driven approach, the data pipeline steps (pre-processing, visualization) are not considered. Moreover, the RNNs struggle with long-term dependencies due to gradient vanishing problem which can be resolved using gating structure of Long short-term memory (LSTM) networks using its specialized gating structure. In [22], authors advocate the integration of deep learning (DL) into MPPT and present deep reinforcement learning (DRL) methods, including deep Q networks (DQN) and deep deterministic policy gradient (DDPG) to optimize the MPP of PV systems under partial shading conditions (PSC), which is beyond the scope of our study. However, DRL techniques such as DQN and DDPG are complex to train and computationally expensive in contrast to the simple implementation and low computational requirements of stack LSTM. The authors in [21] applied a 5-layer bidirectional LSTM (600 neurons) to a 230W solar-wind-battery hybrid system, demonstrating MPPT control but at increased computational intensity. The integration of Bi-LSTM improves accuracy with forward and backward pass layers through advanced network training. However, the complexity of the five-layer deep LSTM network, coupled with the bidirectional information propagation of Bi-LSTM, leads to significant computational overhead and potential inefficiencies in training compared to the proposed two-layer stacked LSTM architecture. A summary of state-of-the-art MPPT controllers for standalone and grid-connected PV systems is presented in Table 1. The table encompasses various parameters, including the mode of operation, complexity, category (such as True MPPT, Simple Estimation MPPT, or Soft Computing MPPT), number and type of sensors used (e.g., voltage (V), current (I), sun irradiance (G), and cell temperature (T)), and cost analysis, derived from an extensive literature survey.

TABLE 1. Comparative assessment of existing MPPT studies.

Ref.	MPPT	Mode	Complexity	Cost	NP-Sensors
True MPP Controllers					
[7]	P&O	SA	L	L	V, I
Simple Estimation MPPT Controllers					
[10]	FOCV	SA	L	L	V
	FSCC	SA	L	L	I
[9]	IC	SA	M	L	V, I
Soft Computing MPPT Controllers					
[12]	FLC	GT	M	M	V, I, G, T
[13]	PSO	SA	M	M	V, I, G, T
[14]	GA	SA	M	M	V, I, G, T
[15]	ANN	SA	M	M	V, I, G, T
[16]	ANN-HC	SA	H	H	V, I, G, T
[17]	ANN-GA	SA	H	H	V, I, G, T
[18]	PSO-ANFIS	GT	H	H	V, I, G, T
[19]	DNN	GT	H	H	V, I, G, T
[20]	RNN	GT	H	H	V, I, G, T
[21]	Bi-LSTM	GT	H	H	V, I, G, T
PR	Stack LSTM	GT	M	M	V, I, G, T

NP: Number of Possible, SA: Standalone, GT: Grid Tied, L: Low, M: Medium, H: High, V: Voltage, I: Current, G: Irradiance, T: Temperature

A comprehensive literature review highlights the challenges faced by traditional, intelligent and hybrid MPPT methods, focusing on their limitations in dynamic environments and slower tracking speed compared to advanced DL-based MPPT techniques. While traditional ML algorithms struggle with time dependency and non-linear relationships, FF-DL methods offer better functionality but may struggle with long-term dependency. RNNs mitigate these challenges but have problems with gradient descent, while LSTM networks address these limitations with specialized memory and gating mechanisms to improve efficiency and performance. In the proposed research, we introduce a holistic stacked LSTM-based MPPT controller for a dual stage grid-connected PV system and reduce the computational complexity in both stages. Compared to existing DL-based MPPT works, our model handles higher power levels (100 kW), uses only two hidden layers with a total of 96 hidden neurons, utilizes *tanh* activation functions for uniform training, integrates dropout layers to avoid overfitting, and adopts a learning rate of 0.05 for stable convergence. This reduced complexity without sacrificing efficiency increases the practical applicability for future researchers. In addition, by prioritizing training using the 80/20 data splitting rule, the proposed research is in line with basic data-driven principles, including data preprocessing (z-score normalization), visualization (bar graphs, histograms, correlation), which have not been considered in past studies.

The main objective of the proposed study is to investigate the potential of DL-LSTM based MPPT controllers in harvesting MPP with maximum efficiency and least complexity by utilizing the aforesaid benefits of LSTM network. Despite the massive potential of DL in time series forecasting applications in energy sector, there are few studies using DL as MPPT in PV solar systems. However, simplifying the complexity remains a challenge and requires careful consideration of computational costs, resources, and convergence issues to assist future researchers in developing real-time DL based MPPT implementation.

The proposed research offers novelty in following aspects: (a) uses stacked LSTM networks as MPPT controllers for two-level grid-connected PV systems, a holistic approach that is not previously studied in the literature; (b) uses only 2 hidden layers and 96 neurons within stacked LSTM to cope with relatively higher power (100 kW), minimizing complexity without sacrificing efficiency; (c) this study conducts a comparative analysis of three Maximum Power Point Tracking (MPPT) models, traditional Perturb and Observe (P&O), Feed-Forward Deep Neural Network (FF-DNN), and the proposed stacked Long Short-Term Memory (LSTM) techniques, using MATLAB to evaluate their performance. The analysis demonstrates the superiority of the proposed stacked LSTM model by comparing it with the widely used, cost-effective, simple, and fast P&O method, as well as the advanced deep learning-based FF-DNN method, highlighting the LSTM model's enhanced accuracy, adaptability, and overall efficiency in tracking the maximum power point, (d) integrates a comprehensive data science and data engineering pipeline including pre-training data processing, visualization, and splitting into the DL-based MPPT methodology, which is an important step in data-driven DL models but has been ignored in past works; (e) realizes DC-link voltage control and active power transfer from PV to grid using a simple PI-based inverter control to achieve complexity reduction.

The main contributions of the proposed research are highlighted below:

- Data Collection: Initially, 1 million data points are randomly collected for both inputs (G, T) using (14) and (15). Corresponding target data for voltage at the MPP is collected using (17). Use of a very large amount of data in training aimed to improve model accuracy and testing on unseen data to ensure it learns rather than memorize patterns to ensure generalizability.
- Data preprocessing: Z-score normalization is used to bring the data to a uniform scale. In comparison to min-max normalization, it not only reduces the effect of outliers, but also improves the convergence speed and training efficiency by centering zeros with a standard deviation of 1, thus providing a more stable and efficient optimization process during model training.
- Exploratory Data Analysis (EDA): EDA is performed on normalized data using statistical techniques and visualization methods such as box plots, histograms, and correlation matrices. These analyses help to understand data distribution, variability, and interrelationships, facilitating pattern identification and the selection of the most appropriate model architecture.
- Hyperparameter tuning: To optimize the LSTM architecture, a manual iterative selective process is performed to investigate different configurations including layer depth and neuron count. The chosen configuration, a two-layer LSTM with 64-32 neurons, strikes a balance between model complexity and performance.
- Model evaluation: The trained model is evaluated using benchmarks such as training loss, mean squared error (MSE), root mean squared error (RMSE), mean absolute error (MAE) and R^2 to assess its prediction accuracy and generalization ability.
- Simulation setup: Simulink/MATLAB is used to simulate three MPPT algorithms: the traditional P&O, the DL-based FF-DNN and the stack LSTM-based MPPT controller. While the P&O controller is implemented directly, the FF-DNN and Stack-LSTM models undergo rigorous pre-processing, training, and testing before being integrated into Simulink. The complexity of the two data-driven models is kept consistent for a fair comparison during the analysis.
- Integration and evaluation: The trained models (FF-DNN and stack LSTM) are integrated into a simulation model of a grid-connected 100 kWp PV system. The comparative analysis of all three MPPT models is

performed based on the maximum power extraction efficiency from a 100 kW PV system.

- The control of dual stage grid-tied PV system: In dual stage grid-tied PV system, the MPP tracking is performed by the DC-DC converter using the proposed stacked LSTM-MPPT controller and the DC-link voltage is regulated by the 3-phase, 3-level Neutral-Point-Clamped (NPC) inverter. The inverter current is conditioned to provide decreased THD to meet the specifications of the grid authorities and active power is transferred to the three-phase microgrid.

The rest of the paper is organized as follows. Section II summarizes the proposed research and model formulation, including the design and formulation of the PV cell, boost converter, LSTM network, and NPC inverter. Section III details the procedures employed in the formulation of the DL model pipeline. This includes collecting input and target data, partitioning the data for training and testing purposes, data normalization, visualization of data distribution, and explicitly designing the DL model, i.e., stacking the LSTM and FF-DNN, while considering the specified hyperparameters. In Section IV, both DL models are trained and tested, the performance is evaluated using MSE, RMSE, MAE, loss, and R2 scores. Section V discusses the LSTM-based MPPT results and presents the PI-based NPC inverter control for grid-connected PV systems. The paper concludes with a summary and outlines future research directions.

II. OVERVIEW AND MODEL FORMULATION OF THE PROPOSED RESEARCH

The proposed dual stage grid-tied PV system comprises two stages; the first stage deals with DL based MPPT controller encompassing a boost converter, whereas the second stage involves DC link voltage regulation and inverter control to ensure power transfer to the grid. The novelty of the proposed work lies in the first stage, and the second stage ensures grid integration with the least complexity. A complete overview of the proposed research is illustrated in **Fig. 3**. This section proceeds with the mathematical model design, formulation, and working of all the important components used in both stages including PV array, boost converter, LSTM-based MPPT controller, and the 3 level NPC inverter.

A. DESIGN AND FORMULATION OF PV CELL

The working principle of a solar PV cell is like the reverse biased PN junction diode. It operates during the sunlight to convert sunlight (photo energy) into electrical energy, and it produces a small ''dark current'' at night. The solar cell is the smallest component of the PV array which adds up to make a PV module that is further joined in parallel and series to get the desired wattage of a PV array. In this study, a total of 96 cells per module, 5 series connected modules per string, and 65 parallel strings are considered to get the desired output power. Considering the simplicity and precision, the single-diode equivalent model of the PV array is considered as indicated in **Fig. 4** [23]. The maximum power of the proposed

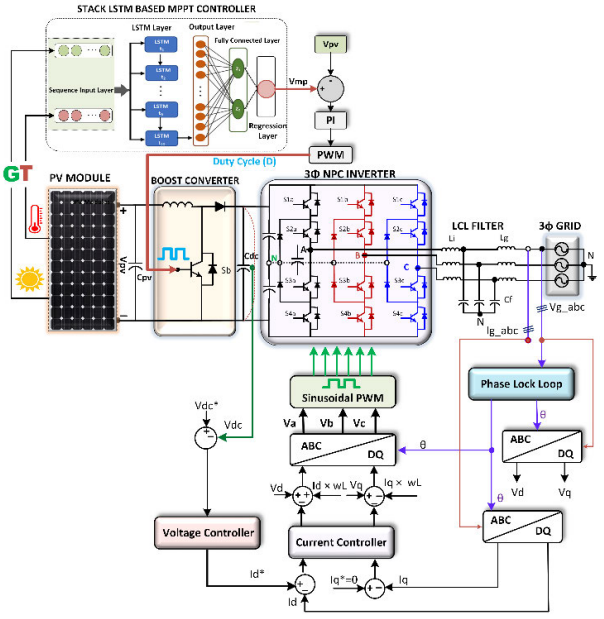

FIGURE 3. The complete schematic diagram of the proposed research.

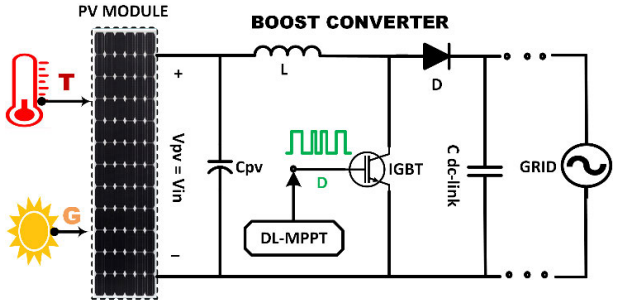

FIGURE 4. The schematic diagram of the boost converter.

TABLE 2. Design parameters of the SunPower TS-SPR-315 PV module.

Symbol	Variable Name	Value
N_s	Number of series-connected modules	5
N_p	Number of parallel-connected modules	65
V_{oc}	Open-circuit voltage	64.2 V
V_{mp}	Maximum power point voltage	54.7 V
I_{sc}	Short-circuit current	5.96 A
A	Ideality factor	0.95
α	I-V temperature coefficient	0.016
β	P-V temperature coefficient	-0.27
P_{max}	Maximum power	315 W
K	Compensation factor	3
N_s	Number of series-connected modules	5

PV array is calculated using the parameters listed in Table 2 as given in (1).

$$P_{pv} = P_{max} N_p N_s = 315 \times 65 \times 5 \approx 102\ kW \qquad (1)$$

Here, I_{ph} is the photocurrent, I_d represents the diode current, I_s denotes shunt current flowing through R_{sh} shunt resistance and I is the net current flowing through R_s series

resistance as modelled by the authors in [24]. The net current is obtained using Kirchhoff's Current Law as shown in (2) [23]. After substituting the values of all the currents, the final output current is modelled in (3).

$$I_{pv} = I_{ph} - I_d - I_{sh} \tag{2}$$

$$I_{pv} = I_{ph} - I_o\{exp[q\,(v + R_s)\,AK\;T_j] - 1\} - \{(v + IR_s)R_{sh}\} \tag{3}$$

Here, I_o is diode junction diffusion current, q is the electric charge ($1.602 \times 10^{-23} C$), K represents the Boltzmann constant ($1.38 \times 10^{-23} J/K$), T_j denotes the junction temperature, and A is the ideality factor.

As the value of R_{sh} is very high so (3) can further be simplified as (4) by neglecting the shunt current. The maximum power equation is modelled in (5) as recommended by the authors in [24].

$$I_{pv} = I_{ph} - I_o\{exp[q\,(v + IR_s)\,AK\;T_j] - 1\} \tag{4}$$

$$I_{pv} = N_p I_{ph} - N_p I_o\{exp[q(v + (R_s N_s / N_p))AKT_j] - 1\} \tag{5}$$

In (5), the solar cell counts in series and parallel configurations are represented by N_s and N_p, respectively as modeled by authors [25].

In the proposed model, 5 series connected modules per string and 65 parallel strings are connected to get the desired 102 kWp output power. The design parameters of the proposed model as applied in the Simulink MATLAB environment are listed in **Table 2** .

B. BOOST CONVERTER DESIGN

In the dual stage grid-connected PV system, a boost converter is vital in the first stage that increases the fluctuating solar PV array voltage (250-280 V) to an 800 V DC bus voltage enabling grid stability and maximum system performance [26]. In the proposed model, the boost converter provides end-to-end system optimization by [25] and [27]: 1) maximizing solar efficiency with dynamic MPPT control, 2) regulating voltage and current levels according to conditions, and 3) boosting to a stable 800 VDC bus suitable for downstream inversion and grid integration. The inclusion of a boost converter in our model is due to its ability to effectively boost the voltage from the PV array to the level required for the inverter. Boost converters are known for their high efficiency, simplicity, and cost-effectiveness. They play a crucial role in maintaining the desired output voltage despite fluctuations in the input from PV panels due to changing irradiance and temperature conditions. This ensures that the maximum power from the PV panels is efficiently converted and transmitted to the grid. Its coordinated optimization, regulation, and power conditioning bridges the MPPT and inverter stages.

The main components in the boost converter topology are the inductor, capacitor, high frequency switches and diode as depicted in **Fig. 5**. The designed values of each electronic component with the corresponding equation are listed in **Table 3** .

TABLE 3. Design parameters of the boost converter.

Symbol	Variable Name	Value
Input Voltage Range	V_{pv}	250-280 V
Output Voltage Range	$V_o = V_i/(1-D)$	0-800 V
Switching Frequency	f_{sw}	5 kHz
Output Current Range	$I_o = V_o/R$	0-125 A
Input Current Range	$I_i = I_i/(1-D)$	0-400 A
Max. Inductor Ripple Current	ΔIL = 5 % (I_o)	6,25 A
Capacitor Ripple Voltage	ΔVC = 5 % (V_o)	40 V

In the presence of rapidly changing weather parameters (G, T), the proposed DL-based LSTM MPPT extracts the voltage at the maximum power point (V_{mp}). The extracted V_{mp} voltage is then compared to solar PV voltage V_{pv} and the error signal is given to PI controller which serves as a reference signal for PWM and controls the switch of the boost converter. When the PV voltage increases, the boost converter switch is activated for proportionally less time per period to reduce the duty cycle (D) to counter the higher input by reducing the switch conduction time to regulate the 800 V DC link; conversely, if the input drops below optimum, the switch on time is extended per cycle to increase duty and maintain the target bus voltage despite lower supply levels. Thus, the proposed MPPT controller dynamically modulates the duty cycle of the boost converter to regulate 800 V DC link voltage in response to solar input voltage fluctuations caused by varying G and T values. The regulation of DC link voltage, inverter operation, and inverter control (voltage and current control) is explained in section II-D.

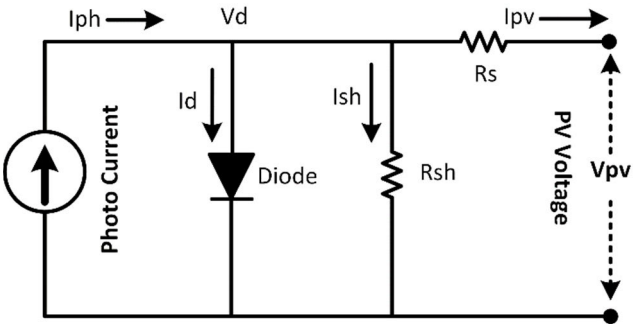

FIGURE 5. Single diode model of a PV cell.

C. DESIGN WORKING AND FORMULATION OF THE LSTM NETWORK

The output power of the solar PV is affected by changes in the values of the parameters G and T. For each combination of G and T, there is a point known as the maximum power point (MPP) where the PV system produces the maximum power output. Since solar cell efficiency is inherently low [28], extracting the maximum power from the PV system under certain G and T conditions is crucial to maximize energy efficiency. This requires the implementation of an MPPT controller to achieve maximum power and increase efficiency

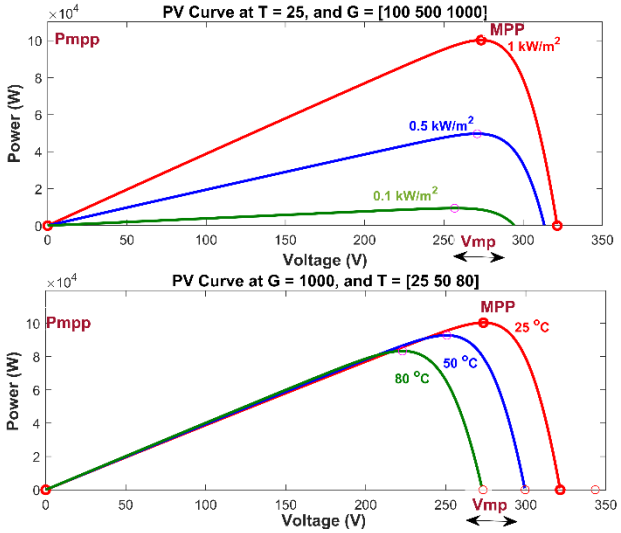

FIGURE 6. PV characteristics of SunPower TS-SPR-315 PV array concerning change in T and G.

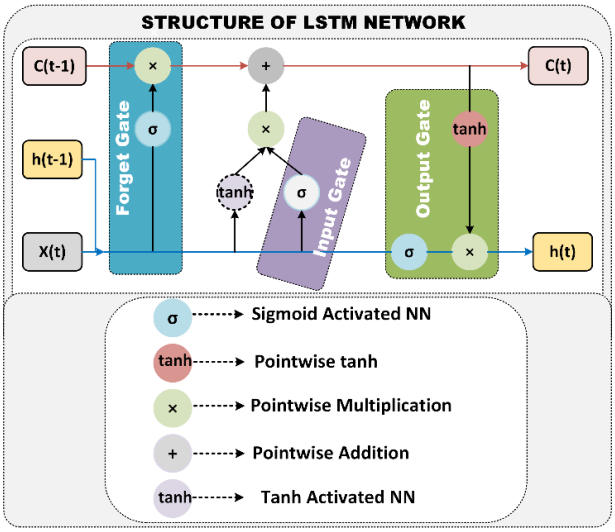

FIGURE 7. The structure and design of a LSTM Cell.

by enabling the PV system to operate at its MPP. The PV characteristics of the proposed SunPower TS-SPR-315 PV module are presented in **Fig. 6**.

The change in G slightly affects the MPP voltage(V_{mp}) value but the change in T significantly affect the value of V_{mp}. Hence, the PV panel's maximum power is accomplished using an adequate proposed stack LSTM MPPT control strategy by controlling the V_{mp} of the PV panel considering the combined effect of G and T on V_{mp} through the coordinated interaction of gating units and memory cells LSTM architecture.

The term ''Deep Learning'' was coined in 1986 and gained importance in the field of ML around 2000, particularly with the emergence of ANNs. DL algorithms, highlighted by [29], use multiple hidden layers for advanced computer learning. While FFNN is simple, its limitations of unidirectional information flow in handling complex time series data led to the development of RNN. However, RNNs face challenges such as exploding and vanishing gradients in extensive time series applications [30]. The gated cell structural model of LSTM introduced by [31] addresses these issues by providing improved accuracy and better results for recursive multi-step time series applications [32]. The structure of an LSTM cell architecture consists of an input gate, a forget gate, a memory cell (memory item or cell state) and an output gate, as shown in **Fig. 7** [31], [33], [34].

The forget gate f_t makes that determination if information should be saved or forgotten from the previous time step $t-1$. The sigmoid σ function keeps its value between 0→Forget and 1→Keep as modelled in (6). The input gate extracts the important input data information at the current time t and categorizes the information as 1→Important and 0→Not Important as modelled in (7). In the intermediate cell state, input gate information is given to the tanh activation function which regulates the cell state value between 1 and -1 as shown in (8). The cell state will decide to store or drop the information (1→store) and (0→drop) by multiplying the information of the previous cell state with forget gate. The subsequent hidden state is completed by the output gate as modelled in (9).

$$f_t = \sigma\left(W_f X_t + W_f S_{t-1} + b_f\right) \tag{6}$$
$$i_t = \sigma\left(W_i X_t + W_i S_{t-1} + b_t\right) \tag{7}$$
$$\bar{C} = \tanh\left(W_i X_t + W_i S_{t-1} + b_t\right) \tag{8}$$
$$O_t = \sigma\left(W_o X_t + W_o S_{t-1} + b_o\right) \tag{9}$$

The current cell state at time t depending on the previous cell state (8) is listed in (10). The hidden state at time step t is given in (11). The cell state and hidden state at time t are the LSTM cell's output. The hidden state at time t is responsible for the time series prediction.

$$C_t = i_t \bar{C} + f_t C_{t-1} \tag{10}$$
$$h_t = O_t \tanh(C_t) \tag{11}$$

In the above equations (6)-(11), $x = x_1, x_2, \ldots x_T$ is the vector of inputs, $h = h_1, h_2, \ldots h_T$ is the hidden vector, and $Y = y_1, y_2, \ldots y_T$ is the output vector modeled at time $T = 1 - t$. In addition, f_t is the forget gate, i_t is the input gate, $\bar{C}$ represents the intermediate cell state, O_t is the output state, σ is the sigmoid activation function, tanh is the hyperbolic tan activation function, W, X, S, b represent weights, inputs, states, and bias of the respective gates [35]. The mathematical forms of the sigmoid and tanh activation functions are presented in (12) and (13), respectively.

$$\sigma(x) = \frac{1}{1 + e^{-x}} \tag{12}$$
$$\tanh(x) = \frac{e^{x} - e^{-x}}{e^{x} + e^{-x}} \tag{13}$$

Finally, the cell state C_t and the hidden state h_t outputs of LSTM are then propagated to the next hidden layer. The iterative process continues until the error approaches the

predefined target. By learning and optimizing the model's weights and bias terms, the LSTM network minimizes the deviation between its output and the actual training samples.

D. NPC INVERTER DESIGN AND FORMULATION

The three-phase 3-level NPC inverter is the key element of the second stage that boosts the DC voltage level output by the MPPT controller supported by the boost converter. The 3-level inverter was selected for its superior efficiency and improved output waveform quality compared to conventional 2-level inverters. It minimizes voltage stress and switching losses, providing cleaner and more stable power required for grid-connected applications and compliance with grid standards. The three-phase grid-connected inverter converts DC input power into three-phase AC power, making it suitable for grid integration [36]. The three-phase inverter consists of three legs with four switches, four freewheeling diodes, and 2 clamping diodes each, for a total of 12 switches and 18 diodes for all phases as shown in **Fig. 8**. In **Fig. 8**, the input side DC voltage is represented by the PV array which is the boosted PV voltage (DC link voltage). This configuration allows precise control over the current flowing between each phase terminal and the DC source.

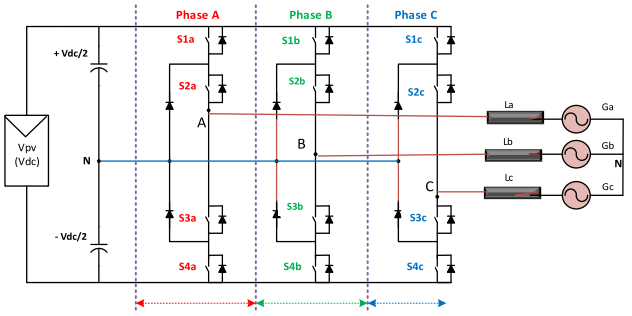

FIGURE 8. The configuration of three-phase 3-level NPC inverter.

The PV-generated voltage (250-280 V) is boosted to 800 V DC using a boost converter controlled by the proposed stack LSTM MPPT controller, the NPC inverter with a DC bus voltage of 800 V produces three voltage levels (+Vdc/2, 0, -Vdc/2) corresponding to (400 V, 0 V, -400 V). Triggering the upper switch S1a connects Phase A to the positive DC bus and produces a voltage of +Vdc/2. Conversely, activating the lower switch S3a produces a voltage of -Vdc/2 by connecting Phase A to the negative DC bus. The coordinated operation of the switches and diodes ensures the precise voltage levels listed in **Table 4** and offers efficient grid injection.

The control strategy applied to the inverter consists of two cascaded loops, (a) the inner current control loop to regulate the grid current and ensure its enhanced quality for grid integration, and (b) the outer control loop is the voltage control to regulate DC bus voltage and balance the power flow in the grid-connected PV model as shown in **Fig. 9**. The three-phase grid currents and voltages are measured, and Clark's transformation converts three-phase system (in *abc* frame) to two components in stationary reference frame ($\alpha\beta$)

TABLE 4. The switching control of the 3 phase 3 level NPC inverter.

Phase	S1	S2	S3	S4	Vo
A	ON	OFF	OFF	ON	+Vdc/2
A	OFF	OFF	ON	ON	-Vdc/2
A	ON	OFF	ON	OFF	0 V
B	ON	OFF	OFF	ON	+Vdc/2
B	OFF	OFF	ON	ON	-Vdc/2
B	ON	OFF	ON	OFF	0 V
C	ON	OFF	OFF	ON	+Vdc/2
C	OFF	OFF	ON	ON	-Vdc/2
C	ON	OFF	ON	OFF	0 V

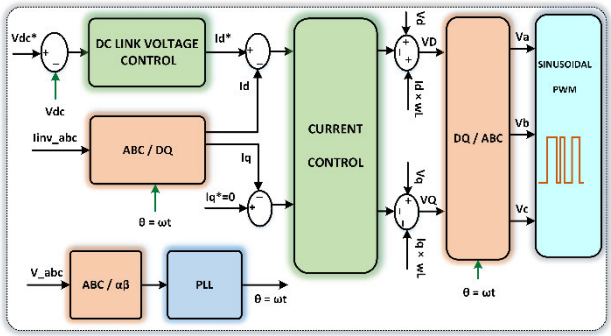

FIGURE 9. The control strategy of the grid integrated inverter.

as modelled in (14). This is followed by Park's transformation modeled in (15) that helps to rotate components in the $\alpha\beta$-frame synchronously to get DC values of the control variables.

$$\begin{bmatrix} v_\alpha \\ v_\beta \end{bmatrix} = \frac{2}{3}\begin{bmatrix} 1 & -\frac{1}{2} & -\frac{1}{2} \\ 0 & \frac{\sqrt{3}}{2} & -\frac{\sqrt{3}}{2} \end{bmatrix}\begin{bmatrix} v_a \\ v_b \\ v_c \end{bmatrix} \tag{14}$$

The transformed voltage signal is then given to the PLL block that determines grid voltage angle to be used for generating synchronous reference frame signals. The phase angle used for the $abc-dq$ transformation module as modeled in (15) is obtained from the PLL block.

$$\begin{bmatrix} v_d \\ v_q \end{bmatrix} = \begin{bmatrix} cos\theta & sin\theta \\ -sin\theta & cos\theta \end{bmatrix}\begin{bmatrix} v_\alpha \\ v_\beta \end{bmatrix} \tag{15}$$

In the current control, the three-phase grid current is transformed using $abc-\alpha\beta$ block and then i_d and i_q currents are obtained through $\alpha\beta - dq$ transformation block and compared with the reference d-axis i_d^* and q-axis i_q^* currents and the error are fed to the respective PI controller [37]. The PI controller's output gives v_d^* and v_q^* reference voltages which are then converted to a three-phase reference voltage signal using inverse transformation $dq-abc$. This three-phase reference voltage signal is compared with a 10 kHz carrier signal using Sinusoidal PWM and generates the control pulses for the NPC inverter.

III. DATA PROCESS PIPELINE STEPS FOR DL MODELS

This section describes the mathematical model and graphical results of the sequential steps involved in the implementation

of the DL algorithm (proposed stacked LSTM and FF-DNN). All ML and DL algorithms start with rigorous data collection, followed by data segmentation, preprocessing (including z-score normalization), visualization (using bar graphs, histograms, and correlation analyses) and subsequent stages including DL model design and hyperparameter selection, followed by model training and testing. Finally, performance evaluation is accomplished using MSE, RMSE, MAE, loss and R2 metrics.

A. INPUTS AND TARGET DATA COLLECTION

In the proposed grid-connected PV system, G and T are the two inputs and the voltage at MPP *Vmp* is the target output. The quality and nature of data have been verified from reputed sources such as the National Renewable Energy Laboratory (NREL), European Solar Radiation Atlas, and World Radiation Data Centre (WRDC) and *G* data ranges from 0 to 1000 W/m^2 depending on geographical location. After analyzing the data points from the above sources within the relevant constraints, this study generated the replicated input data of *G* and *T* using (16) and (17) as proposed by the authors in [15].

$$\mathrm{G} = [(G_{max} - G_{\min}) \times rand] + G_{\min} \tag{16}$$

$$\mathrm{T} = [(T_{max} - T_{\min}) \times rand] + T_{\min} \tag{17}$$

In addition to the input (G, T) data, initial target data for V_{mp} are also required to train the supervised DL models. The authors in [20] modelled T input dependent target dataset as modelled in equation (18).

$$V_{mp} = V_{mp(STC)} + \beta\,(T_s - T) \tag{18}$$

To model the V_{mp} as a function of G and T, this study utilizes a modified form of equation (18) shown in (19), incorporating influences of both inputs (G, T) on the target output V_{mp}. The target data samples are first collected across varying G and T conditions in Simulink MATLAB using a SunPower TS-SPR-315 PV module. Linear regression via the least squares method is then applied to this dataset to deduce optimal alpha (α) and beta (β) constants for the module that provides a mathematical relationship between the independent variables and the target V_{mp}.

$$V_{mp} = V_{mp(STC)} + \beta\,(K * T - T_s) + \alpha(1 + G) \tag{19}$$

$$I_{mp} = \left\{ I_{mp(STC)} + \left[\frac{G}{G_s} (1 + \alpha(T - T_s)) \right] \right\} \tag{20}$$

$$P_{mp} = \{ V_{mp} * I_{mp} \} \tag{21}$$

The PV cell current modelled by (20) and (21) shows the power at maximum power point as the product of current and voltage. In this research, raw G, T, and V_{mp} ranges span 0-1000 W/m^2, 20-80 °C, and 250-280 V respectively and the complete input dataset obtained using equations (16), (17), and (19) is demonstrated in **Fig. 10**. The equations from (16) to (21) are used to formulate the inputs and target for the DL based LSTM MPPT controller (stack LSTM and FF-DNN). Subsequently, these input data of T and G leveraged to train and test the DL based MPPT controller for the given grid-tied PV system. The target value V_{mp} depends on both inputs (T and G) to the PV array or MPPT controller. The higher the G value, the higher the *Vmp*, while a higher T value decrease V_{mp}.

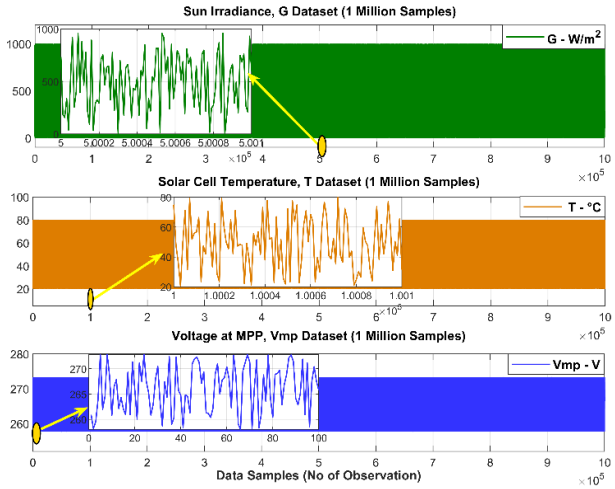

FIGURE 10. The complete input dataset used in DL based LSTM.

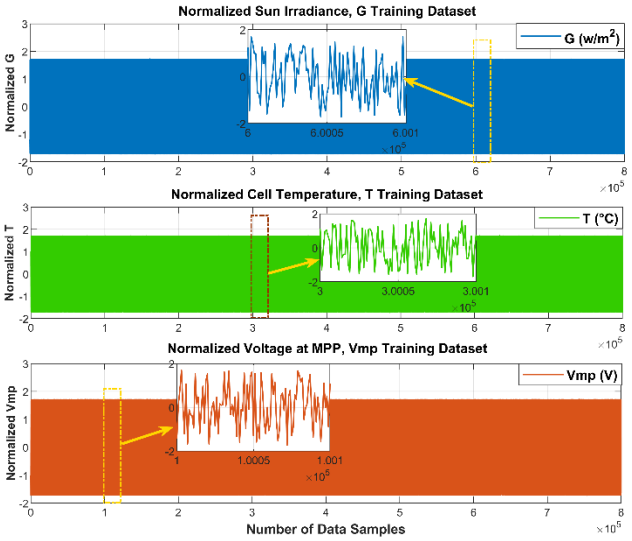

FIGURE 11. Initial 80 % data used for training of both the DL models.

B. TRAIN AND TEST DATASET SEGMENTATION

The collected input data for (G, T) using (16) and (17), and target data (V_{mp}) using (20) is partitioned into training and test subsets using 80/20 split rule which is the general approach adopted in DL algorithms [38]. The sequence consists of one million (1,000,000) data points (observations). From the beginning, 80% of the total dataset is used for training and the remaining 20% is used for testing and validation. Then, the training and testing datasets are pre-processed separately before training the proposed stacked LSTM and FF-DNN models.

C. DATA NORMALIZATION

In DL frameworks, normalization of the input and target dataset constitutes a crucial preprocessing step before training the DL model. This research uses z-score standardization as modelled in (22), which centres the distributions around the sample mean (μ) while scaling them by the standard deviation (σ), accounting for the dispersion of values and able to deal with outliers that often occur in real-world PV data [39].

$$\text{Zscore} = (\text{X} - \mu)/\sigma(1) \tag{22}$$

Here, z is the normalized or ''standardized'' value, x is the raw value, μ is the mean and σ is the standard deviation of the sample population.

The G, T and *Vmp* training data, ranging from 0-1000 W/m^2, 20-80 °C, and 250-280 V respectively, are normalized using Z-score normalization to obtain a uniform distribution between -1.7 and 1.7 on the y-axis, while the x-axis boundaries (80% quantile) remain unchanged, providing balanced normalization without skewness [40]. The normalized test data having the rest of the last 20% of the data samples is demonstrated in **Fig. 12**.

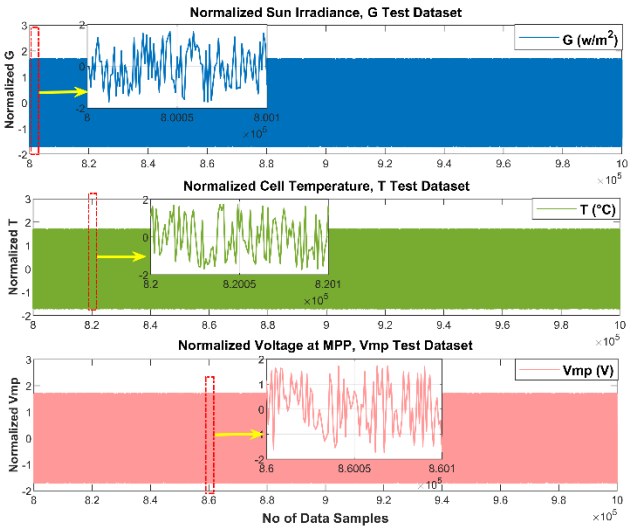

FIGURE 12. Last 20 % data samples used as test dataset for both the DL models.

D. DATA VISUALIZATION

After data acquisition, segmentation, and z-score normalization, data insights are aggregated through graphical representations, including histograms for dispersion, box plots for statistical distribution, and correlation coefficient matrices using (23) to comprehend variable relationships.

$$r = Cov(X, Y)/(\sigma x * \sigma y) \tag{23}$$

Fig. 13 shows the uniform distribution of the unstandardized data set, where the X-axis represents parameter values (G: 0-1000 W/m^2, T: 20-80 °C and *Vmp*: 250-280 V) and the Y-axis represents frequencies.

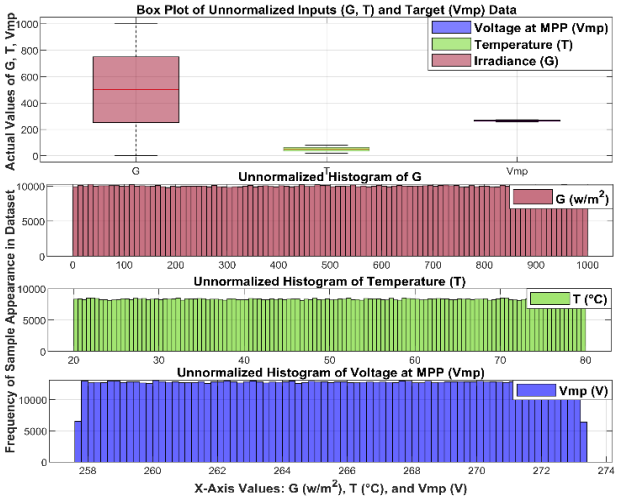

FIGURE 13. Bar chart and histogram-based visualization of the un-normalized complete Inputs and Target dataset.

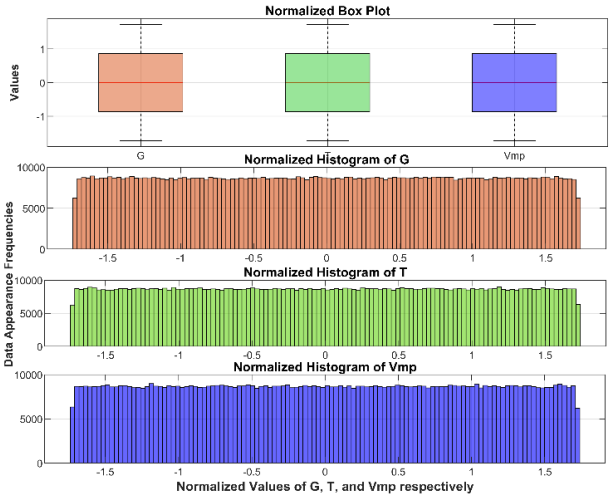

FIGURE 14. Bar chart and histogram-based visualization of the Normalized complete Inputs and Target dataset.

This consistency ensures the diversity of the data representation and validates the prediction range. A graphical representation of the normalized data using histograms and box plots with a standardized scale (-1.7 to 1.7) on the z-axis is presented in **Fig. 14**. Histogram analysis helps to understand the behaviour of the modified data set, where values close to -1 or 1 indicate proximity to the mean, while other values deviate from the mean in the range -1.7 to 1.7.

A precise understanding of the distribution patterns increases the reliability of subsequent analyses and validates the validity of the preprocessing step. The correlation matrix shown in **Fig. 15** describes the main relationships between the input variables (G, T) and the target variable (*Vmp*). Both G and T exhibit a weak positive correlation (0.23), indicating a slight increase in T with higher values of G, while there is no correlation between T and G (0.00).

The strong positive correlation between G and Vmp (0.73) indicates that with increasing G values there is a tendency

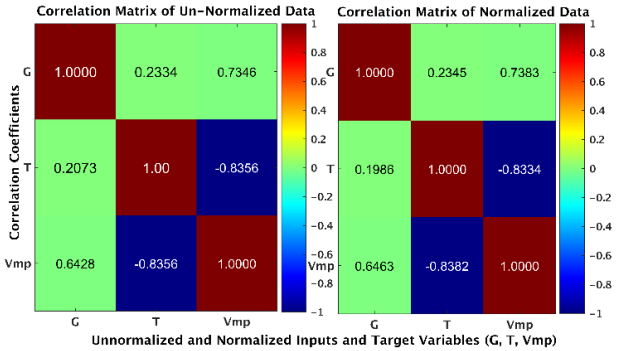

FIGURE 15. Inputs and target dependencies and data relationship analysis using correlation matrix.

for an increase in *Vmp*. Also, the strong negative correlation between T and *Vmp* (-0.83) indicates a decrease in *Vmp* with increasing T values. Correlations such as the strong positive correlation between G and *Vmp* and the negative correlation between T and *Vmp* guide the design of a DL-based stack LSTM MPPT controller with inputs (G, T) and a single output *Vmp*.

Given that data collection, data pre-processing, and visualization have been successfully completed, this section proceeds to the implementation of the design architecture and hyperparameter selection of the proposed stacked LSTM and benchmark FF-DNN model as MPPT controllers, followed by training the designed models on the pre-processed dataset.

E. DL MODEL DESIGN AND HYPERPARAMETERS

In this paper, two DL models, (a) the proposed stack LSTM MPPT model and (b) the FF-DNN MPPT model, are simulated and the results are benchmarked.

1) DESIGN OF PROPOSED STACK LSTM MPPT

Determining the optimal LSTM configuration requires balancing model complexity and long-term PV data dependencies. The 1 million sample time series has multiple time-scale patterns that require specialized LSTM memory cells over feed-forward or simple RNN networks [41].

The 2-layer, 64-32 neuron stacked LSTM MPPT architecture was analytically selected by sweeping candidate topologies from 1-4 layers with 32-128 units per layer, and monitoring validation error convergence over 50 epochs. Negligible RMSE improvements were observed for networks exceeding the chosen architecture, despite their substantial additional computational overhead. Since the research aims for an efficient topology optimizing accuracy and simplicity, the streamlined proposed model achieves equivalent performance to the overdesigned alternatives. By systematically profiling the design space to optimize for efficacy and efficiency, selection of this compact yet accurate MPPT architecture is analytically justified through structured error analysis rather than being arbitrary. The MPPT stacked LSTM model incorporates a G-T based input layer, two processing LSTM layers with 64 and 32 units to extract

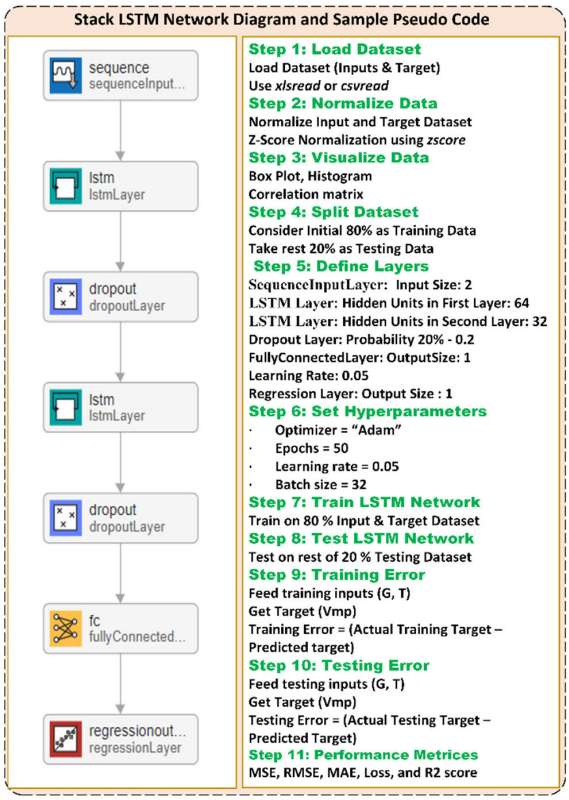

FIGURE 16. The network design and sample pseudo code of the proposed stack LSTM Network.

temporal relationships, 20% dropout regularization to prevent overfitting, an MPP voltage output layer, and a regression loss function enabling backpropagation. The MATLAB pseudo code and the sequence layered structure of the 2 layered stack LSTM are presented in **Fig. 16**.This streamlined framework balances predictive accuracy and computational efficiency for grid-connected systems. Careful calibration targets the 250-280 V MPP voltage range from z-score normalized inputs. Implementation employs the Adam optimizer (learning rate 0.05) for weight updating, an 80/20 data split, L2 regularization, 50 training epochs, and a batch size of 32 to ensure convergence without overfitting as listed in **Table 5** .

TABLE 5. Design and Hyperparameters selection of Stack LSTM network.

Parameter	Value
First Layer	64 Hidden Neurons
Second Layer	32 Hidden Neurons
Learning Rate	0.05
Decay Mechanism	Applied
Initialization	He Initialization
L2 Regularization	0.0001
Optimization Algorithm	Adam
Mini Batch Size	32
Train-Test Split	80-20

The structured topology and training optimizations extract complex solar dynamics while optimizing efficacy and

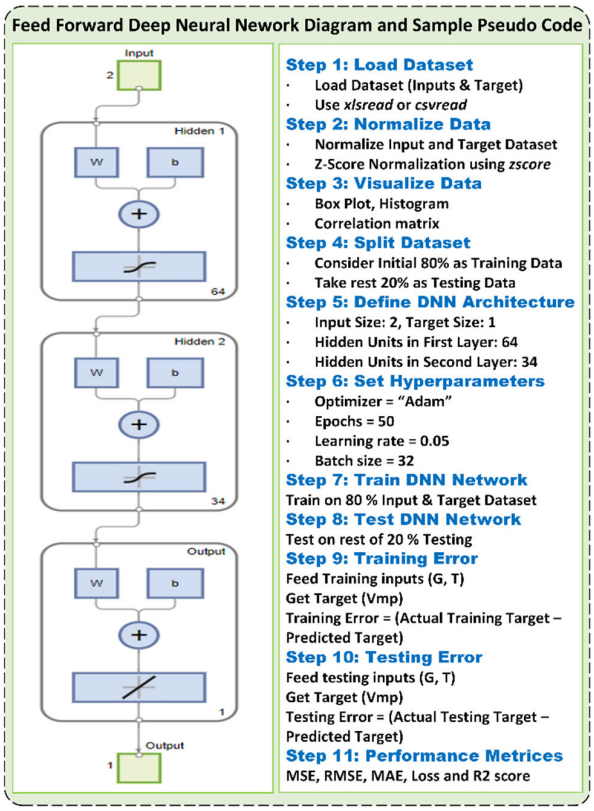

FIGURE 17. The network design and sample pseudo code of the FF-DNN network.

simplicity. The hyperparameters are fine-tuned according to the input data (G, T) and the target *Vmp* to maximize accuracy. The effectiveness of our chosen parameters is highlighted by their compliance with established principles that promote a balanced convergence rate and effective overfitting prevention.

2) DESIGN OF FEED FORWARD DNN MPPT

The structured fully connected FF-DNN network as MPPT controller adopts similar design considerations as the proposed stack LSTM, including two hidden layers with 64 and 32 hidden neurons, same hyperparameter fitting, and z-score normalized G and T inputs. This streamlined topology avoids over-parameterization while skilfully capturing complex PV dynamic data to extract maximum power from PV array under variable G and T values. The processing layers apply the nonlinear tanh activation function, chosen for its proven effectiveness in representing complex renewable energy input-output relationships without gradual fading. The network design of FF-DNN in Simulink with pseudo-MATLAB code is presented in **Fig 17**. Likewise, the network design and hyperparameter selection of the FF-DNN and the proposed stack LSTM comprise the same design complexity to ensure direct performance contrast, emphasizing the specialized memorization temporal processing capabilities of LSTM networks.

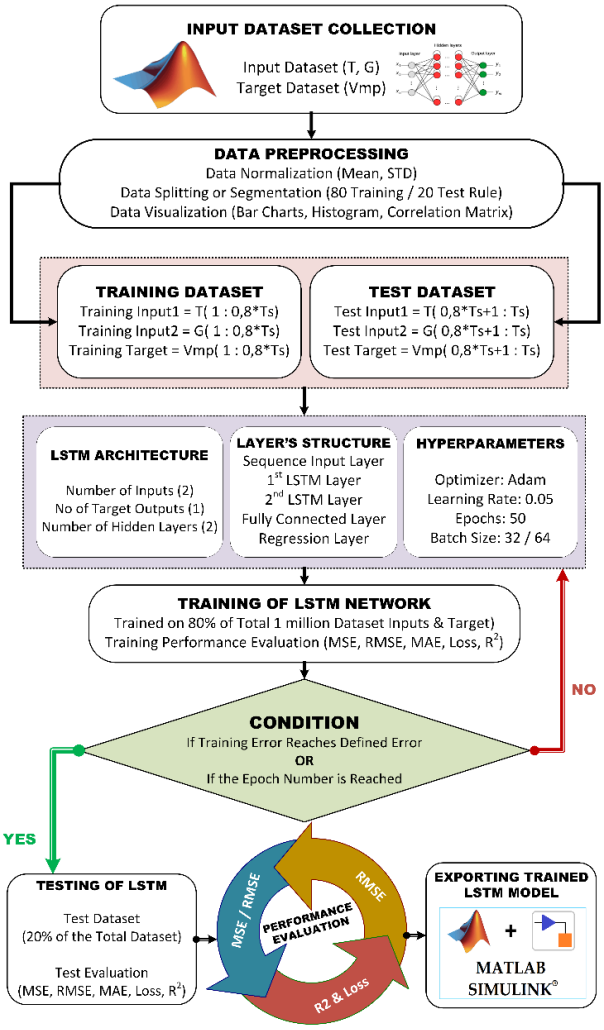

FIGURE 18. All steps including data preprocessing, training testing, and performance evaluation of the DL models.

IV. TRAINING OF THE DEEP LEARNING MODELS

After completing key steps, such as acquiring data (G, T, *Vmp*), segmentation, z-score normalization, and visualization (bar charts, histograms, correlations), both the DL models are designed and proper hyperparameters are selected. The proposed stack LSTM and FF-DNN models are ready for training on the normalized 80% of the data which is one of the most crucial steps in the ML and DL models. The training process is executed on hardware featuring an Intel i7-7600U CPU with a clock speed of 2.80 GHz and 16 GB of RAM, utilizing the MATLAB 2023 Deep Network Designer Toolbox. The main steps involved in the training process are presented in **Fig. 18**.

1) TRAINING AND TESTING OF THE STACK LSTM MPPT

In the training process, the LSTM network continuously improves in terms of RMSE as shown in **Fig. 19**. The training process of LSTM gradually reduces the RMSE over 50 training epochs and reaches a remarkable RMSE of

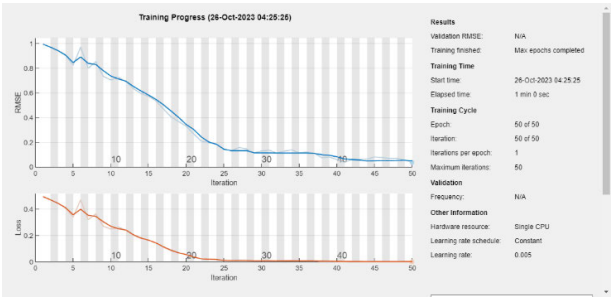

FIGURE 19. The RMSE reduction in training process of the LTSM network with increasing epochs.

0.048265 in the last epoch. Furthermore, the loss function values of LSTM are below 0.05. The improved performance is also ensured using all important performance evaluation metrics. The performance of the proposed stacked LSTM MPPT as listed in **Table 6** shows that the MSE is 0.0023295, RMSE is 0.048265 and MAE is 0.033978, which is very close to the ideal value of zero. The Loss Function Value is consistently below 0.05 and the R-squared (R^2) regression value is an impressive 0.99768, very close to the ideal value of 1. These metrics collectively demonstrate the effectiveness of the Stack LSTM and reveal that it makes accurate predictions of the target with minimal error. The R^2 value is close to 1, indicating the high explanatory power of the model and confirming its reliability for maximum power extraction and forecasting purposes in grid-connected PV systems. The training of the proposed stack LSTM model on 80% of one million data (G, T, *Vmp*) gives a small training error of 0.048 as shown in **Fig. 20**.

TABLE 6. Performance evaluation of the proposed trained stack LSTM MPPT control model.

Performance Metric	Value
Mean Squared Error	0.002329
Root Mean Squared Error	0.048265
Mean Absolute Error	0.033978
Loss Function Value	< 0.05
R-squared (R^2) Score	0.99768

This indicates the close matches between the predicted *Vmp* and the actual *Vmp* target output which ensures the robustness of the trained stack LSTM MPPT for future testing with unseen G, T data. The trained stack LSTM model is then tested on the remaining 20% of the one million data (G, T, *Vmp*). The error between the actual test target *Vmp* and the predicted target *Vmp* is also close to 0.048 as shown in **Fig. 21**. This close match between the actual and predicted target value ensures higher efficiency and robustness of the model for the other unseen data of the variable inputs G and T of the MPPT in the PV array.

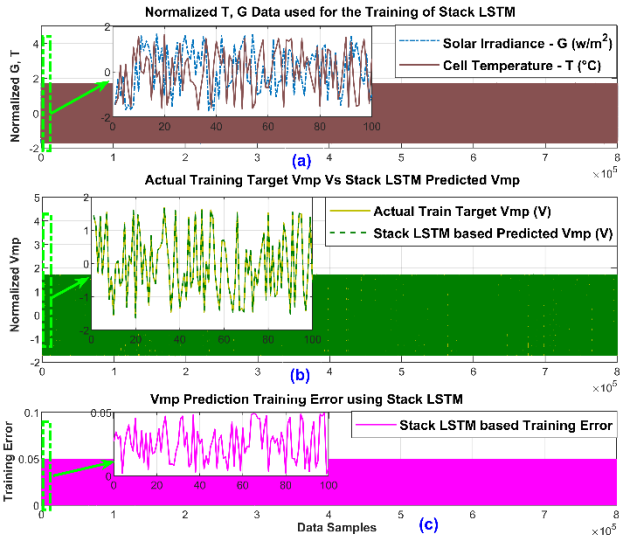

FIGURE 20. The training inputs-target, the actual vs predicted target, and the training error of the LSTM network.

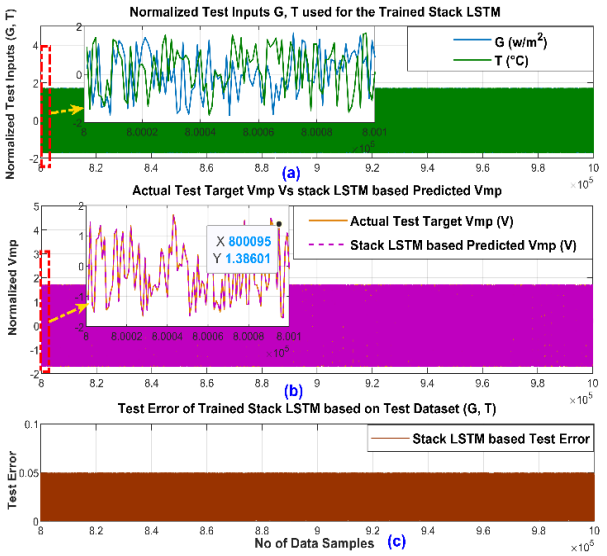

FIGURE 21. The comparison of the actual and the LSTM based predicted test target to compute the testing error.

2) TRAINING TESTING OF THE FF-DNN MPPT

The FF-DNN model is also trained on the same 80% of the 1 million datasets, the *Xtrain* and *Ytrain* dataset vectors are used to "train" the DNN network. The performance of the model is evaluated using MSE, RMSE, MAE, loss function, and R^2 regression. After 50 training epochs, the MSE decreased to 0.18561 and the loss decreased below 0.1 as shown in **Fig. 22**.

These reductions indicate increasingly accurate predictions in line with the actual target *Vmp* values. Low final MSE and loss values also indicate optimal training of the FFDNN model and enable effective generalization for the new unseen data. The DNN model also shows significant performance

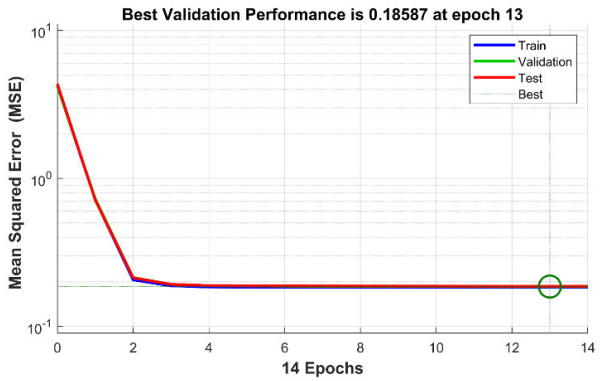

FIGURE 22. The MSE reduction in training process of the DNN network with increasing epochs.

metrics with an MSE of 0.18561, RMSE of 0.43083, MAE of 0.33843 and a loss function value consistently below 0.1 (see **Table 7**).

TABLE 7. Performance evaluation of the trained FF-DNN MPPT control.

Performance Metric	Value
Mean Squared Error	0.18561
Root Mean Squared Error	0.43083
Mean Absolute Error	0.33843
Loss Function Value	< 0.1
R-squared (R^2)	0.80438

The R-squared (R^2) value is 0.80438. Although DNN converges faster than LSTM, it exhibits higher error values in the MSE, RMSE and R-squared metrics than LSTM. While both models exhibit efficient predictions, LSTM, with its lower error values, proves to be more efficient in predicting the target variable *Vmp* to extract maximum power for grid-connected PV systems.

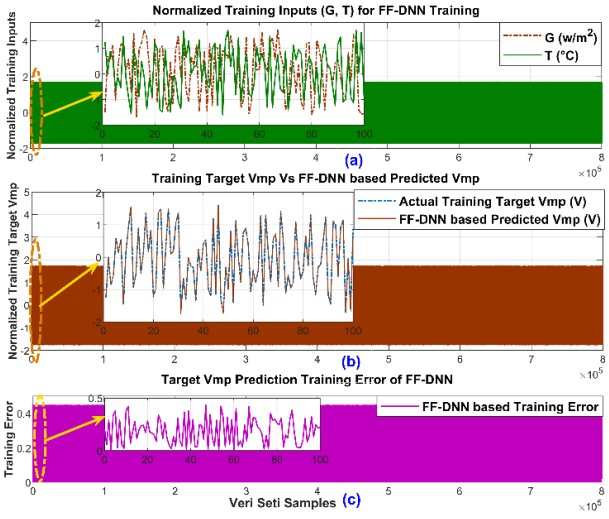

FIGURE 23. The comparison of the actual and the DNN based predicted training target to compute the training error.

The normalized training inputs (G, T) are fed into the designed two-layer DNN architecture as shown in **Fig. 23**.

The predicted outputs are then compared with the actual training targets to calculate the training error.

The training error falls within a small range of 0.45, indicating that the error is of a small magnitude close to zero. This indicates robustness for future testing on other unknown data sets. Although an MSE value of 0.18 is noticed during the training process, the RMSE value is almost 0.45, which is the same as the error between the predicted and actual target *Vmp* values.The trained DNN model is tested on the inputs fed to the DNN (G, T) and the remaining 20% of the unseen data to obtain the predicted outputs.

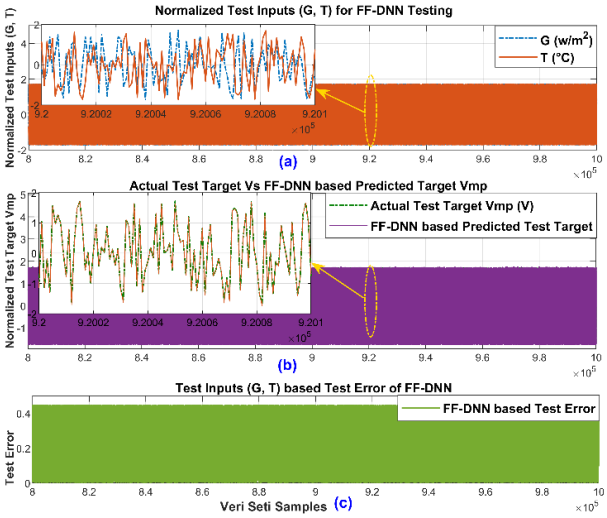

FIGURE 24. The comparison of the actual and the DNN based predicted testing target to compute the testing error.

The comparison with real test targets reveals errors in the range of 0.45 and provides a good prediction as shown in **Fig. 24**. However, the test error of the LSTM is 0.048, which is much smaller than the DNN test error and provides higher efficiency for maximum power extraction in PV systems. In this comparative analysis, few most important performance metrics, including MSE, RMSE, MAE, MAE, Loss and R^2 are used to provide a comprehensive assessment of the accuracy and reliability of the model. These metrics provide a robust assessment by measuring various aspects of prediction error and goodness of fit.

3) PERFORMANCE COMPARISON OF LSTM AND DNN

The performance parameters (MSE, RMSE, MAE, and loss) near zero suggest that the model is making accurate predictions, and the differences between predicted and actual values are minimal. In addition, the R^2 score near 1 show that the model is capturing much of the information in the data, and the predictions are closely aligned with the actual values. The comparative performance of the proposed stack LSTM and FF-DNN as demonstrated in **Fig. 25** shows significant MPPT efficiency of the stacked LSTM over FF-DNN with

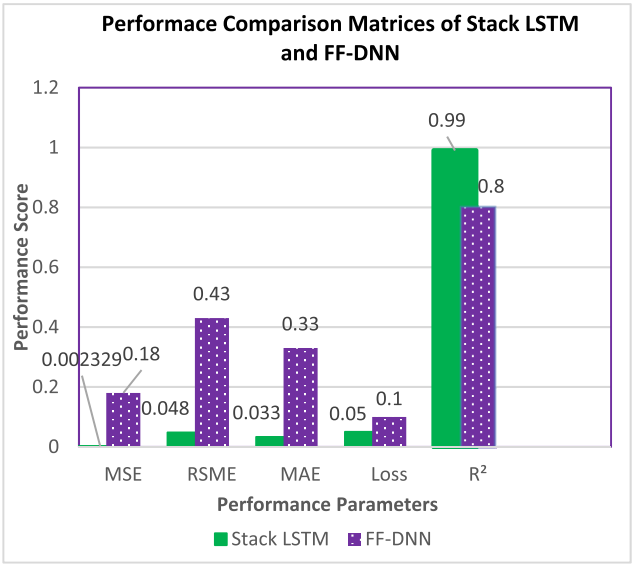

FIGURE 25. The performance score-based comparison of both the proposed stack LSTM and FF-DNN model.

approximately 10 times better MSE (0.002 vs. 0.186), 9 times better RMSE (0.048 vs. 0.431) and MAE (0.034 vs. 0.338), and halved loss. The 0.99 higher R^2 score of stack LSTM than 0.8 of FF-DNN ensures the proposed model's predictions are closely related to actual target values.

In contrast to the limitation of feed-forward topology in modelling complex climate-energy interactions, LSTM leverages specialized memory components designed to capture the intermittency of the sun, which can be attributed to natural repeatability to preserve both transient and long-term meteorological dynamics. This simple yet high-fidelity 2-layer model outperforms state-of-the-art methods in terms of loss performance, forecast reliability and applicability, verified by 99% test efficiency. Trained and then successfully tested, the models are ready to be imported into Simulink/MATLAB to be integrated with the Simulink model of a 100 kW grid-connected PV system.

V. RESULTS AND DISCUSSION

This section provides the simulation setup used for the proposed research, followed by the simulation results and a discussion of the first and second stages of the grid-connected PV system.

A. SIMULATION SETUP

This study employs a simulation-based approach to compare the performance of three MPPT controllers for a 100 kW grid-connected PV system using Simulink/MATLAB 2023© including P&O, FF-DNN, and the proposed Stack LSTM MPPT controller. The P&O algorithm, as a non-data-driven approach, is directly implemented in Simulink and integrated into the grid-tied PV system model. Conversely, DL-based MPPT models (stacked LSTM and FF-DNN) are designed and trained using the deep network designer toolbox in MATLAB® on an Intel i7-7600U CPU (2.80 GHz) with 16GB RAM. Effective training of both models is achieved after testing and evaluation based on performance metrics including MSE, RMSE, MAE, loss, and R^2 are utilized for comparative analysis. The analysis reveals superior performance of the LSTM model, evidenced by higher R^2 values (closer to 1) and slower error metrics nearing to zero. Subsequently, both trained DL models are exported to Simulink MATLAB and integrated with the 100 kW SunPower TS-SPR-315 grid-connected PV module to maximize the PV power. The proposed grid-connected PV system has two phases: (a) in the first stage, the novelty of the proposed work lies in extracting the maximum power from the 100 kW PV array using a stacked LSTM MPPT controller, while (b) in the second stage, the DC link voltage regulation and the active power transferred to the grid are achieved through simple PI empowered current and voltage controllers. Given the computational complexity of the DL algorithm in the first stage, simple PI controllers to ensure reduced complexity are considered in the second stage. In this study, the schematic diagrams are made using Microsoft Visio 2016, the bar chart and pie chart are created using Microsoft Excel, and the rest of all the simulation graphics are accomplished through MATLAB 2023©.

B. SIMULATION RESULTS OF THE FIRST STAGE OF THE GRID-TIED PV SYSTEM

The trained DL models are imported into Simulink for integration with the Simulink model of a 100 kW grid-connected PV system. G and T signals are applied for a 1.5 s period at a sampling rate of 1 MHz, generating approximately 1.5 million samples. To comprehensively evaluate and visualize the performance under varying conditions, the G and T signals are divided into 9 different states (1 to 9) over 1.5 unit, with each state corresponding to a specific behaviour after 0.15 second increments on the timeline, as shown in **Fig. 26**. This allows the models to be tested with fluctuating G and T inputs that represent real-world operating dynamics. Each state represents a specific G and T behaviour, allowing detailed analysis of the MPPT controller response. Cases 1-4 focus on the effects of individually decreasing/increasing G and T while other parameters are constant. Cases 5-7 analyse the combined effects of simultaneous G and T change. Finally, cases 8-9 provide insight into real-world operational dynamics by presenting random fluctuations in one variable while the other is constant at STC. To simplify the analysis, one variable is held constant while the other is varied. This approach isolates the impact of each specific input on the target, allowing for a clearer understanding of their individual effects.

Variable input signals G and T are fed to the SunPower TS-SPR-315 PV array and the corresponding voltage, current and power responses under these fluctuating conditions are shown in **Fig. 27**. The analysis confirms the direct (inverse) proportional relationship between G (T) and the output PV power. In addition, the calculated power of the PV array is

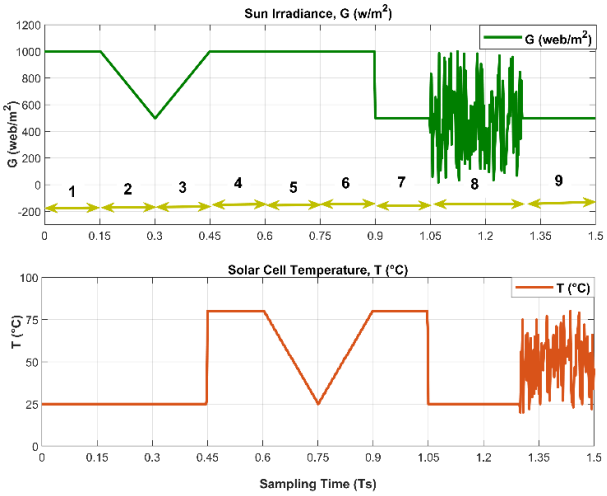

FIGURE 26. The inputs (G and T) signals which are categorized into 9 states are used for both the trained DL models.

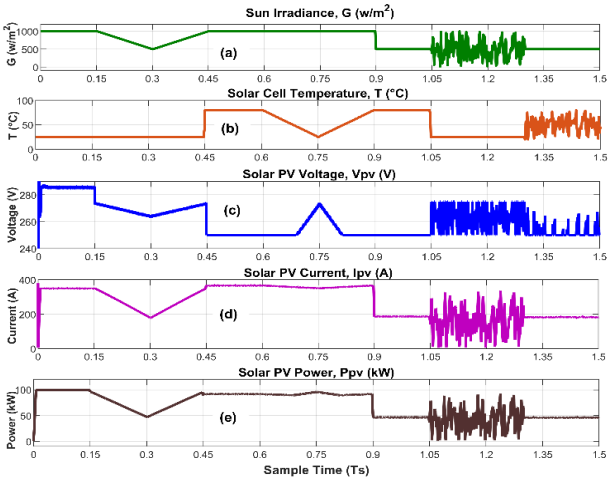

FIGURE 27. The voltage current and power of the SunPower TS-SPR-315 PV module against G and T variations.

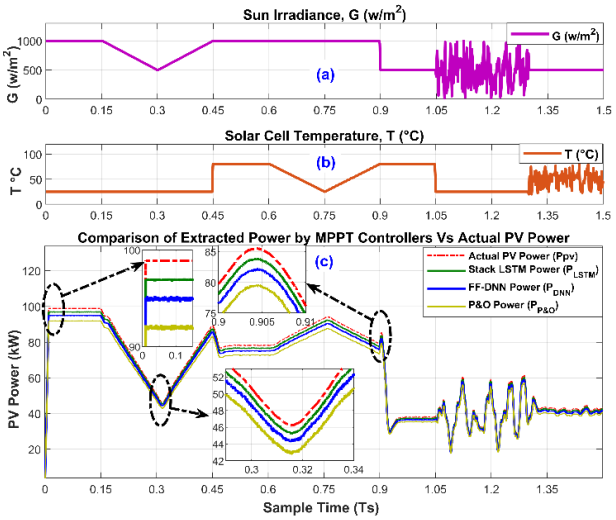

FIGURE 28. Comparison of the proposed stack LSTM MPPT controller with FF-DNN and P&O for effective maximum power extractions.

102 kW (315 × 65×5) under STC values of G and T. The actual maximum power output of this PV module under the applied G and T values is **99.87** kW at STC values of G and T. To get this maximum available power of the PV array, the performance comparison results of the proposed stack LSTM, FF-DNN, and P&O MPPT controllers are detailed in the following section.

Simulation results comparing the maximum power extraction from the PV array of three different MPPT controllers, including two DL-based MPPT algorithms (the proposed Stacked LSTM and FF-DNN) and the conventional P&O MPPT, are presented in **Fig. 28**.

The DL approaches follow a data-driven methodology including acquisition, segmentation, visualization, training, and testing, whereas P&O uses PV voltage and current as input to control the boost converter duty cycle with a fixed step size of 0.001. In DL algorithms, a voltage control strategy is applied for MPPT by subtracting the voltage at the maximum power point (*Vmp*) to operate the PV voltage (*Vpv*) at this Vmp level. Thus, the output Vmp predicted by the MPPT controllers is compared with the actual Vpv and the difference error signal is fed to a PI controller to regulate the duty cycle of the 5 kHz IGBT switch in the boost converter. The maximum output power achieved using the proposed Stacked LSTM MPPT controller is 98.7 kW, surpassing both the DNN (96.3 kW) and P&O (94.5 kW) MPPT controllers.

Being trained on a large dataset of 1 million samples allows the DL algorithms (LSTM and DNN) to converge early to the target solution by exploiting the knowledge gained from oscillating around the MPP as exhibited in the P&O approach. This inherent fluctuation in P&O produces lower average power output. Furthermore, the feedback and memory units in the LSTM architecture enable faster learning and superior maximum performance, whereas feed forward DNNs process information in only one direction. Thus, the Stacked LSTM MPPT controller outperforms other DL and conventional MPPT techniques. The MPPT controller dynamically adjusts the boost converter duty cycle to align *Vpv* with *Vmp*, ensuring optimal PV system performance. The voltage range of 250-280 V *Vpv*, influenced by varying G and T inputs, serves as the boost converter input and the 800 V DC link is the output voltage of the boost converter as shown in **Fig. 29**. The error signal reflecting the difference between *Vpv* and *Vmp* is processed by a PI controller. This PI controller regulates the IGBT switch duty cycle in the range 0.6-0.7 and maintains a consistent 800 V DC bus voltage. When *Vpv* increases, the MPPT reduces duty to maintain 800 V and conversely, increases duty for lower *Vpv*. This strategic duty cycle setting prevents excessive idle power losses and eliminates overheating problems.

In the first stage, the proposed Stacked LSTM MPPT controller empowered by the PV array and boost converter outperformed both DNN (96.3 kW) and P&O (94.5 kW)

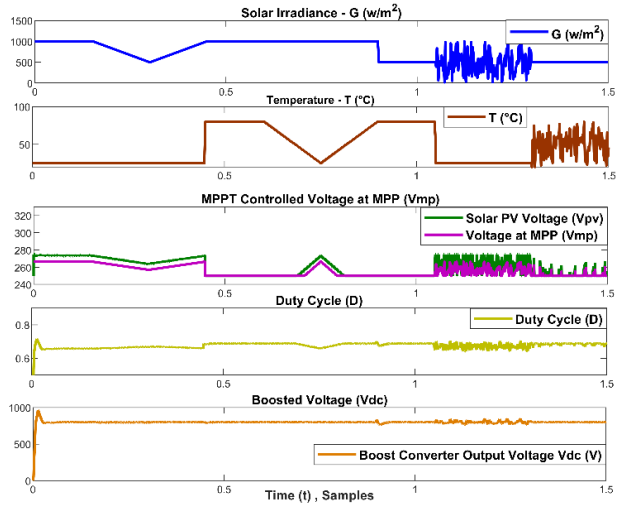

FIGURE 29. Determining the PV voltage, boost converter voltage, and the corresponding duty cycle for varying inputs G and T.

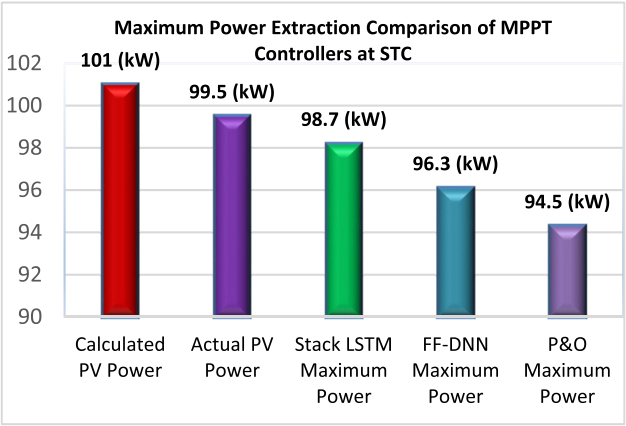

FIGURE 30. Maximum PV Power harvesting comparison among the proposed stack LSTM, FF-DNN, and P&O MPPT controllers.

MPPT approaches by achieving 98.7 kW of the 99.8 kW power generated by the PV system as shown in **Fig. 30**.

Thus, the grid-connected inverter control results in the second stage are realized using only the proposed stacked LSTM-based MPPT controller. Furthermore, the boost converter regulated by the LSTM MPPT provides a DC link voltage of 800 V that varies slightly with varying G and T values. The inverter control further smooths this DC input using PI-enabled voltage and current controllers, ensuring its suitability as a constant ripple-free source for the 3-phase NPC inverter.

C. SIMULATION RESULTS OF THE SECOND STAGE OF THE GRID-TIED PV SYSTEM

Among the analysed stacked LSTM, FF DNN and P&O MPPT controllers, the stacked LSTM MPPT shows the highest efficiency and accuracy, so the subsequent inverter simulations continue with the power extracted by the proposed MPPT controller.

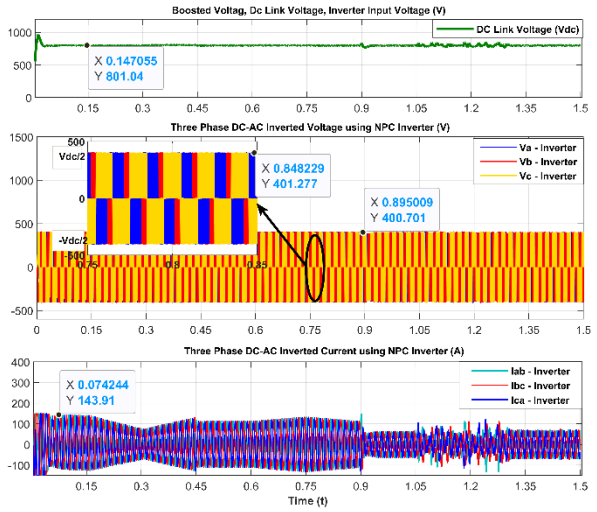

FIGURE 31. The output current and voltage of the 3 phase 3 level NPC inverter for 800 V DC Link bus voltage.

First, the PV array (250-280 V) is stepped up to 800 V using the boost converter empowered with a stacked LSTM MPPT controller.

The 800 V DC link voltage fluctuates slightly due to fluctuating G (0-1000 W/m^2) and T (20-80°C). In the second stage, individual PI current and voltage controllers further smooth the 800 V DC link feeding the 3-phase, 3-level NPC inverter to reduce the harmonics injected into the grid. The NPC inverter is designed for 400 V/144 A output to meet 100 kW demand according to 400 V grid standards as shown in **Fig. 31**. This robust two-stage grid-connected system configuration, together with the details of the inverter control ensures efficient and uninterrupted transfer of PV power to the microgrid [42]. The output waveforms of the three-phase 400 V line-to-line voltage (230 V phase voltage) and 144A current alongside grid synchronization, globally recommended for microgrid integration, are realized corresponding to the fluctuating values of G and T, shown in **Fig. 32**. In droop control, the reactive current is assumed to be zero, hence only active power transfer is obtained using (24). The grid voltage and current waveforms are in phase, which gives $\theta = 0$, Cos $\theta = 1$, so out of 98.7 kW extracted power by the proposed stack LSTM, the 98.4 kW of active power is transferred from the PV array to the microgrid.

$$P = \sqrt{3} \times V \times I \cos\theta = 98.4\text{kW} \tag{24}$$

In the first stage, the stacked MPPT controller extracted 98.7 kW of the maximum total PV power of 99.5 kW at STC. In the second stage, 98.4 kW of active power is successfully transferred to the grid, providing a 400-volt line-to-line, 230-volt line-to-neutral, and 144A microgrid as shown in **Fig. 33**.

In addition, the DC link voltage is regulated to 800 volts to reduce current harmonic injection and improve reliability in accordance with the IEEE 1547 grid standard; grid synchronization and power factor unity are achieved as the grid voltage and grid current were in phase; and 98.4 kilowatts

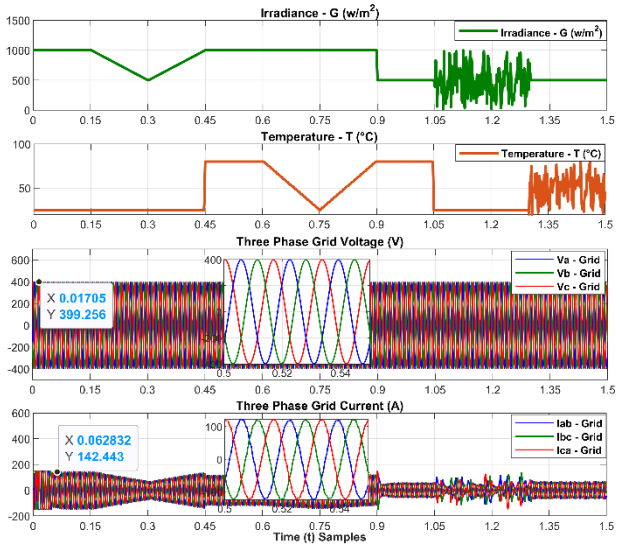

FIGURE 32. Three phase synchronized grid voltage and current with respect to variable G and T values.

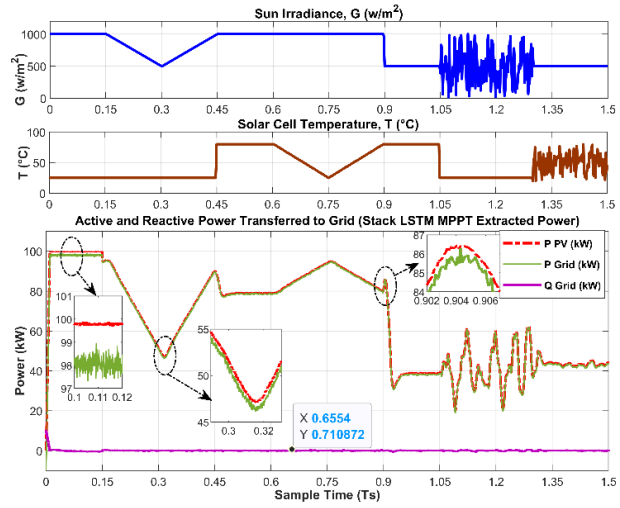

FIGURE 33. The PV array generated 99.5 kW, the proposed stack LSTM MPPT controller harvested 98.7 kW, and 98.4 kW is transferred from the PV system to the 3-phase grid.

of active power is transferred to the three-phase microgrid and complies with global microgrid voltage standards.

VI. CONCLUSION AND FUTURE DIRECTIONS

This research proposed and simulated an LSTM-based MPPT controller for a 100 kW grid-connected PV system in MATLAB/Simulink. The stacked LSTM topology demonstrated precise real-time solar dynamics modelling by achieving 98.7 kW of the 99.5 kW maximum PV power, surpassing feedforward deep neural network and perturb and observe methods. With a mean squared error of just 0.002 and R2 score of 0.99 on the comprehensive dataset, the LSTM significantly outperformed alternatives in capturing complex $G-T$ relationships. DC-DC conversion and DC-AC inversion based on 3-phase 3-level PWM inverter enabled reliable grid integration, successfully transferring 98.4 kW of the 98.7 kW MPPT-optimized power at 400 V line-line, 230 V line-neutral, and 144A. By combining DL and power electronics techniques, this study confirms and advances the prospects for AI-enabled large-scale solar PV energy harvesting. The modelling, accuracy, adaptation capabilities, and grid integration efficacy evidenced in simulation collectively validate LSTM networks' effectiveness for advancing PV system optimization. Our simulation-based study presents a simplified stacked LSTM-based MPPT control, which optimizes computational complexity, convergence time, and cost. After manual approached based hyperparameter selection, a 2-layer stack LSTM architecture is considered, incorporating 64 and 32 neurons in respective layers, along with a batch size of 32 and the Adam optimizer, outperforms traditional and DL based MPPT methods like P&O and FF-DNN respectively.

In our study, we reduced the complexity by optimizing the PV-side LSTM-MPPT architecture and grid-side inverter control. Considering the data availability, the training process of proposed research is performed on hardware with Intel i7-7600U CPU with a clock speed of 2.80 GHz and 16 GB RAM using MATLAB 2023 Deep Network Designer Toolbox. However, inherent limitations of DL models seem as a key challenge demanding substantial computational resources, influenced by dataset size for training efficiency. Real-world deployment may require powerful GPUs, cloud resources, or specialized hardware. Challenges also arise in integrating grid-tied inverters: ensuring compatibility, reliable prediction of optimal power points under dynamic grids, and seamless integration with existing control systems. Despite these constraints, proposed Stacked LSTMs offer potential for enhanced efficiency and adaptability, but at lower complexity, making them ideal for real-time operations.

Future work involves validating proposed techniques in a real scenario. The recommendations for real-time implementation of stacked LSTM MPPT include collecting data from actual PV power plants operating in real time to increase the practical applicability. Current study uses 1 million data points generated for inputs G and T using underlying PV equations (14) and (15) but these datasets can be collected from real PV plants. Furthermore, inputs such as temperature and irradiance data can be collected from sensors such as pyranometers for irradiance and thermocouples or RTDs for temperature. Further strategies can be explored for mitigating the impact of partial shading (PSC) on the proposed MPPT controller, potentially through incorporating additional sensors for PSC detection or investigating P-V curve scanning algorithms. Collaboration with industry partners can improve the verification process by facilitating access to sensors and real PV installations (which are also direct beneficiaries). While our study highlights technical advances in MPPT algorithms and PV system functions, future research should consider broader socio-economic and environmental impacts. In real-world applications, factors such as accessibility, affordability and environmental sustainability need to be

considered to ensure equitable and sustainable deployment. Finally, the scalability of DL-based MPPT controllers in real PV power plants depends on several factors, including the availability and quality of data, the complexity of the DL model, computational resources, and the ability to cope with extreme operating conditions. To which, techniques such as transfer learning, data augmentation and hardware acceleration can be explored to overcome these challenges. Our work emphasizes simplicity and scalability to enable adaptation to different PV configurations and environmental conditions, and to ensure efficiency and effectiveness in different applications and operating scenarios.

REFERENCES

[1] R. M. Elavarasan, G. M. Shafiullah, S. Padmanaban, N. M. Kumar, A. Annam, A. M. Vetrichelvan, L. Mihet-Popa, and J. B. Holm-Nielsen, "A comprehensive review on renewable energy development, challenges, and policies of leading Indian states with an international perspective," *IEEE Access*, vol. 8, pp. 74432–74457, 2020, doi: 10.1109/ACCESS.2020.2988011.

[2] H. Ritchie, P. Rosado, and M. Roser, "Energy production and consumption," Global Change Data Lab, England Wales, U.K., Tech. Rep., 2024.

[3] T. Jiang, P. Ji, Y. Shi, Z. Ye, and Q. Jin, "Efficiency assessment of green technology innovation of renewable energy enterprises in China: A dynamic data envelopment analysis considering undesirable output," *Clean Technol. Environ. Policy*, vol. 23, no. 5, pp. 1509–1519, Jul. 2021, doi: 10.1007/s10098-021-02044-9.

[4] M. M. Gulzar, A. Iqbal, D. Sibtain, and M. Khalid, "An innovative converterless solar PV control strategy for a grid connected hybrid PV/wind/fuel-cell system coupled with battery energy storage," *IEEE Access*, vol. 11, pp. 23245–23259, 2023, doi: 10.1109/ACCESS.2023.3252891.

[5] M. Makkiabadi, S. Hoseinzadeh, A. Taghavirashidizadeh, M. Soleimaninezhad, M. Kamyabi, H. Hajabdollahi, M. M. Nezhad, and G. Piras, "Performance evaluation of solar power plants: A review and a case study," *Processes*, vol. 9, no. 12, p. 2253, Dec. 01, 2021, doi: 10.3390/pr9122253.

[6] O. Ayan and B. E. Turkay, "Techno-economic comparative analysis of grid-connected and islanded hybrid renewable energy systems in 7 climate regions, Turkey," *IEEE Access*, vol. 11, pp. 48797–48825, 2023, doi: 10.1109/ACCESS.2023.3276776.

[7] S. Salman, X. Ai, and Z. Wu, "Design of a P-&-O algorithm based MPPT charge controller for a stand-alone 200W PV system," *Protection Control Modern Power Syst.*, vol. 3, no. 1, pp. 1–8, Dec. 2018, doi: 10.1186/s41601-018-0099-8.

[8] F. Muñoa, "Characterization of a chromosomal mutant that blocks hemolysin excretion in *Escherichia coli*," *FEMS Microbiol. Lett.*, vol. 56, no. 2, pp. 167–172, Dec. 1988, doi: 10.1016/0378-1097(88)90184-x.

[9] M. Alsumiri, "Residual incremental conductance based nonparametric MPPT control for solar photovoltaic energy conversion system," *IEEE Access*, vol. 7, pp. 87901–87906, 2019.

[10] M. M. Shebani, T. Iqbal, and J. E. Quaicoe, "Comparing bisection numerical algorithm with fractional short circuit current and open circuit voltage methods for MPPT photovoltaic systems," in *Proc. IEEE Electr. Power Energy Conf. (EPEC)*, Oct. 2016, pp. 1–5.

[11] A. K. Podder, N. K. Roy, and H. R. Pota, "MPPT methods for solar PV systems: A critical review based on tracking nature," *IET Renew. Power Gener.*, vol. 13, no. 10, pp. 1615–1632, Jul. 2019, doi: 10.1049/iet-rpg.2018.5946.

[12] H. Rezk, M. Aly, M. Al-Dhaifallah, and M. Shoyama, "Design and hardware implementation of new adaptive fuzzy logic-based MPPT control method for photovoltaic applications," *IEEE Access*, vol. 7, pp. 106427–106438, 2019.

[13] K. Ishaque, Z. Salam, M. Amjad, and S. Mekhilef, "An improved particle swarm optimization (PSO)-based MPPT for PV with reduced steady-state oscillation," *IEEE Trans. Power Electron.*, vol. 27, no. 8, pp. 3627–3638, Aug. 2012, doi: 10.1109/TPEL.2012.2185713.

[14] S. Hadji, J.-P. Gaubert, and F. Krim, "Real-time genetic algorithms-based MPPT: Study and comparison (theoretical an experimental) with conventional methods," *Energies*, vol. 11, no. 2, p. 459, Feb. 2018, doi: 10.3390/en11020459.

[15] R. B. Roy, M. Rokonuzzaman, N. Amin, M. K. Mishu, S. Alahakoon, S. Rahman, N. Mithulananthan, K. S. Rahman, M. Shakeri, and J. Pasupuleti, "A comparative performance analysis of ANN algorithms for MPPT energy harvesting in solar PV system," *IEEE Access*, vol. 9, pp. 102137–102152, 2021, doi: 10.1109/ACCESS.2021.3096864.

[16] S. Allahabadi, H. Iman-Eini, and S. Farhangi, "Fast artificial neural network based method for estimation of the global maximum power point in photovoltaic systems," *IEEE Trans. Ind. Electron.*, vol. 69, no. 6, pp. 5879–5888, Jun. 2022, doi: 10.1109/TIE.2021.3094463.

[17] A. A. Kulaksiz and R. Akkaya, "A genetic algorithm optimized ANN-based MPPT algorithm for a stand-alone PV system with induction motor drive," *Sol. Energy*, vol. 86, no. 9, pp. 2366–2375, Sep. 2012, doi: 10.1016/j.solener.2012.05.006.

[18] S. Siddaraj, U. R. Yaragatti, and N. Harischandrappa, "Coordinated PSO-ANFIS-based 2 MPPT control of microgrid with solar photovoltaic and battery energy storage system," *J. Sensor Actuator Netw.*, vol. 12, no. 3, p. 45, May 2023, doi: 10.3390/jsan12030045.

[19] A. Ab-BelKhair, J. Rahebi, and A. A. M. Nureddin, "A study of deep neural network controller-based power quality improvement of hybrid PV/wind systems by using smart inverter," *Int. J. Photoenergy*, vol. 2020, pp. 1–22, Dec. 2020, doi: 10.1155/2020/8891469.

[20] R. Srinivasan and C. R. Balamurugan, "Deep neural network based MPPT algorithm and PR controller based SMO for grid connected PV system," *Int. J. Electron.*, vol. 109, no. 4, pp. 576–595, Apr. 2022, doi: 10.1080/00207217.2021.1914192.

[21] C. Kumar, G. Subramaniam, and J. Jasper, "A novel ROA optimized bi-LSTM based MPPT controller for grid connected hybrid solar-wind system," *COMPEL-Int. J. Comput. Math. Electr. Electron. Eng.*, vol. 42, no. 2, pp. 378–401, Jan. 2023, doi: 10.1108/compel-11-2021-0453.

[22] B. C. Phan, Y.-C. Lai, and C. E. Lin, "A deep reinforcement learning-based MPPT control for PV systems under partial shading condition," *Sensors*, vol. 20, no. 11, p. 3039, May 2020, doi: 10.3390/s20113039.

[23] M. Rokonuzzaman, M. Shakeri, F. A. Hamid, M. K. Mishu, J. Pasupuleti, K. S. Rahman, S. K. Tiong, and N. Amin, "IoT-enabled high efficiency smart solar charge controller with maximum power point tracking—Design, hardware implementation and performance testing," *Electronics*, vol. 9, no. 8, p. 1267, Aug. 2020, doi: 10.3390/electronics9081267.

[24] M. G. Molina and E. J. Espejo, "Modeling and simulation of grid-connected photovoltaic energy conversion systems," *Int. J. Hydrogen Energy*, vol. 39, no. 16, pp. 8702–8707, May 2014, doi: 10.1016/j.ijhydene.2013.12.048.

[25] N. Mohan, T. M. Undeland, and W. P. Robbins, *Power Electronics: Converters, Applications, and Design*. Hoboken, NJ, USA: Wiley, 2003.

[26] R. Ayop and C. W. Tan, "Design of boost converter based on maximum power point resistance for photovoltaic applications," *Sol. Energy*, vol. 160, pp. 322–335, Jan. 2018, doi: 10.1016/j.solener.2017.12.016.

[27] M. Rajkumar and A. Rathinam, "Design and experimental investigation of zeta converter fed reduced switch multi-stage grid connected boost MLI," *J. Electr. Eng. Technol.*, vol. 19, no. 1, pp. 361–371, Jan. 2024, doi: 10.1007/s42835-023-01517-9.

[28] K. El Mezdi, A. El Magri, A. Watil, I. El Myasse, L. Bahatti, R. Lajouad, and H. Ouabi, "Nonlinear control design and stability analysis of hybrid grid-connected photovoltaic-battery energy storage system with ANN-MPPT method," *J. Energy Storage*, vol. 72, Nov. 2023, Art. no. 108747, doi: 10.1016/j.est.2023.108747.

[29] R. Indrakumari, T. Poongodi, and K. Singh, "Introduction to deep learning," in *EAI/Springer Innovations in Communication and Computing*. Cham, Switzerland: Springer, 2021, doi: 10.1007/978-3-030-66519-7_1.

[30] N. Bhoj and R. S. Bhadoria, "Time-series based prediction for energy consumption of smart home data using hybrid convolution-recurrent neural network," *Telematics Informat.*, vol. 75, Dec. 2022, Art. no. 101907, doi: 10.1016/j.tele.2022.101907.

[31] S. Hochreiter and J. Schmidhuber, "Long short-term memory," *Neural Comput.*, vol. 9, no. 8, pp. 1735–1780, Nov. 1997.

[32] M. S. Karabinaoglu, B. Çakir, M. E. Basoglu, A. Kazdaloglu, and A. Guneroglu, "Comparison of deep learning and regression-based MPPT algorithms in PV systems," *Turkish J. Electr. Eng. Comput. Sci.*, vol. 30, no. 6, pp. 2319–2338, Sep. 2022, doi: 10.55730/1300-0632.3941.

[33] V. Lendave, "LSTM vs GRU in recurrent neural network: A comparative study," AIM, India, Tech. Rep., 2021.
[34] J. Patterson and A. Gibson, *Deep Learning: A Practitioner's Approach*, vol. 53, no. 9. Sebastopol, CA, USA: O'Reilly Media Inc., 2019.
[35] J. Duan, P.-F. Zhang, R. Qiu, and Z. Huang, "Long short-term enhanced memory for sequential recommendation," *World Wide Web*, vol. 26, no. 2, pp. 561–583, Mar. 2023, doi: 10.1007/s11280-022-01056-9.
[36] M. H. Muhammad and H. Rashid, "Power electronics: Devices, circuits and applications," *TIDEE, TERI Inf. Dig. Energy Environ.*, vol. 20, no. 2, p. 277, 2021.
[37] M. H. Mahlooji, H. R. Mohammadi, and M. Rahimi, "A review on modeling and control of grid-connected photovoltaic inverters with LCL filter," *Renew. Sustain. Energy Rev.*, vol. 81, pp. 563–578, Jan. 01, 2018, doi: 10.1016/j.rser.2017.08.002.
[38] A. Gholamy, V. Kreinovich, and O. Kosheleva, "Why 70/30 or 80/20 relation between training and testing sets: A pedagogical explanation," *Int. J. Intell. Technol. Appl. Stat.*, vol. 11, no. 2, pp. 105–111, 2018.
[39] S. Bhanja and A. Das, "Impact of data normalization on deep neural network for time series forecasting," 2018, *arXiv:1812.05519*.
[40] A. Asesh, "Normalization and bias in time series data," in *Digital Interaction and Machine Intelligence* (Lecture Notes in Networks and Systems). Cham, Switzerland: Springer, 2022, doi: 10.1007/978-3-031-11432-8_8.
[41] T. Elsken, J. H. Metzen, and F. Hutter, "Neural architecture search: A survey," *J. Mach. Learn. Res.*, vol. 20, no. 55, pp. 1–21, 2019.
[42] Y. Bektas and H. Karaca, "Red deer algorithm based selective harmonic elimination for renewable energy application with unequal DC sources," *Energy Rep.*, vol. 8, pp. 588–596, Nov. 2022, doi: 10.1016/j.egyr.2022.05.209.

UMAIR YOUNAS received the B.S. and M.S. degrees in electrical and electronics engineering from COMSATS University Islamabad, Abbottabad Campus, Pakistan, in 2013 and 2017, respectively, and the Ph.D. degree in electrical and electronics engineering from Selçuk University, KTUN, Konya, Turkey, in 2024. He successfully completed M.S. research thesis with the University of Sannio, Benevento, Italy. His research interests include artificial intelligence, machine learning, deep learning, solar photovoltaic energy applications in smart grid, industrial, and robotics automation. During the M.S. degree program, he was awarded with the Erasmus Mundus LEADERS Scholarship (Ten-Months Asia-Europe Master's Research Mobility).

AHMET AFSIN KULAKSIZ was born in Eskişehir, Turkey, in 1978. He received the B.S., M.S., and Ph.D. degrees in electrical and electronics engineering from Selçuk University, Turkey, in 1998, 2001, and 2007, respectively. He is currently a Professor with Konya Technical University, Turkey. His current research interests include renewable energy resources, especially power electronics applications in photovoltaic energy systems, artificial intelligence techniques, microgrid, and power quality.

ZUNAIB ALI (Member, IEEE) received the B.Sc. degree in electronic engineering from the University of Engineering and Technology, Peshawar, Pakistan, in 2013, the M.Sc. degree in electrical engineering from COMSATS University Islamabad, Abbottabad, Pakistan, in 2015, and the Ph.D. degree in electrical engineering from Frederick University, Nicosia, Cyprus, in 2018. He is currently a Senior Lecturer with the Division of Electrical and Electronic Engineering, London South Bank University, and a member with London Center of Energy Engineering (LCEE). His research interests include grid synchronization and control methods for distributed renewable energy systems and how such systems can be strategically utilized in applications related to power electronic converters and consequently in smart grids and microgrids. He was a recipient of the 36-Month Erasmus Mundus European Union Research Scholarship for Ph.D. studies and is also the Gold Medalist. He has contributed to several research projects on renewables, electric vehicles, and energy management in a microgrid involving practical demonstration and prototype component design; and generated an income of £674k.